Molecular gas in super spiral galaxies [*]

Ute Lisenfeld[1,2], Patrick M. Ogle[3], Philip N. Appleton[4], Thomas H. Jarrett[5], and Blanca M. Moncada-Cuadri[6]

[1] Departamento de Física Teórica y del Cosmos, Universidad de Granada, 18071 Granada, Spain, e-mail: ute@ugr.es
[2] Instituto Carlos I de Física Téorica y Computacional, Facultad de Ciencias, 18071 Granada, Spain
[3] Space Telescope Science Institute, 3700 San Martin Drive, Baltimore, MD 21218, USA
[4] Caltech/IPAC, 1200 E. California Blvd., Pasadena, CA 91125, USA
[5] Department of Astronomy, University of Cape Town, Private Bag X3, Rondebosch 7701, South Africa
[6] Department of Physics, University of Bath, Claverton Down, Bath, BA2 7AY, UK

ABSTRACT

At the highest stellar masses ($\log(M_*) \gtrsim 11.5\ M_\odot$), only a small fraction of galaxies are disk-like and actively star-forming objects. These so-called 'super spirals' are ideal objects to better understand how galaxy evolution proceeds and to extend our knowledge about the relation between stars and gas to a higher stellar mass regime. We present new CO(1-0) data for a sample of 46 super spirals and for 18 slightly lower-mass ($\log(M_*) > 11.0\ M_\odot$) galaxies with broad HI lines – HI fast-rotators (HI-FRs). We analyze their molecular gas mass, derived from CO(1-0), in relation to their star formation rate (SFR) and stellar mass, and compare the results to values and scaling relations derived from lower-mass galaxies. We confirm that super spirals follow the same star-forming main sequence (SFMS) as lower-mass galaxies. We find that they possess abundant molecular gas (mean redshift-corrected molecular gas mass fraction ($\log(f_{\mathrm{mol,zcorr}})$ = -1.36 ± 0.02), which lies above the extrapolation of the scaling relation with stellar mass derived from lower-mass galaxies, but within the relation between f_{mol} and the distance to the SFMS. The molecular gas depletion time, τ_{dep}= M_{mol}/SFR, is higher than for lower-mass galaxies on the SFMS (τ_{dep}= 9.30 ± 0.03, compared to τ_{dep}= 9.00 ± 0.02 for the comparison sample) and seems to continue an increasing trend with stellar mass. HI-FR galaxies have an atomic-to-molecular gas mass ratio that is in agreement with that of lower-mass galaxies, indicating that the conversion from the atomic to molecular gas proceeds in a similar way. We conclude that the availability of molecular gas is a crucial factor to enable star formation to continue and that, if gas is present, quenching is not a necessary destiny for high-mass galaxies. The difference in gas depletion time suggests that the properties of the molecular gas at high stellar masses are less favorable for star formation.

Key words. galaxies: evolution – galaxies: spiral – galaxies:ISM – ISM: molecules

1. Introduction

Considerable progress has been made in recent years in our understanding of how galaxies evolve. For gas-rich disk galaxies, there exists a tight relation between star formation rate (SFR) and stellar mass, usually referred to as the star-forming main sequence (SFMS, e.g., Brinchmann et al. 2004; Elbaz et al. 2007). The slope of this relation is slightly less than unity (in a log-log representation), so that the specific SFR (sSFR = SFR/M_*) decreases with stellar mass, M_*. This relation indicates that spiral galaxies evolve a large fraction of their lifetime along the SFMS by converting a relatively steady gas supply into stars. The molecular gas depletion time (τ_{dep}= M_{mol}/SFR) is surprisingly constant as a function of redshift for galaxies close to the SFMS (Tacconi et al. 2020), indicating that the conditions under which star formation (SF) occurs are very uniform in normal disk galaxies.

At high stellar masses ($\log(M_*) \sim 10.5\ M_\odot$), the growth of disks seems to come to a halt and disk galaxies become more and more rare, whereas spheroidal galaxies become more frequent (Kauffmann et al. 2003). SF seems to become quenched at these high stellar masses. There are several possible explanations for a drastic decrease in SF for high-mass galaxies: Major galaxy

mergers may disrupt disk galaxies and transform them rapidly into elliptical galaxies (Baldry et al. 2004). Increasing feedback from a growing supermassive black hole in an active galactic nucleus (AGN) may shock or eject gas from the galaxy disk, reducing its capacity to form stars (Hopkins et al. 2006; Ogle et al. 2014)). Ram-pressure stripping of the interstellar medium by the intercluster medium in a galaxy cluster can also remove cold gas (Sivanandam et al. 2014). An available cold gas reservoir is furthermore fundamental to maintain SF. A lack of gas or a lack of molecular gas that formed from atomic gas or inefficient SF due to the properties of the molecular gas could all decrease the SFR in a galaxy. The accretion of cold gas onto a galaxy may be stopped when the galaxy halo becomes so massive that accretion shocks develop, interrupting the cold streams of gas needed to replenish the disk (Dekel & Birnboim 2006). The molecular-to-atomic gas mass ratio depends on properties like the midplane pressure in galaxies (Wong & Blitz 2002; Blitz & Rosolowsky 2004, 2006; Leroy et al. 2008) and variations in these parameters among galaxies can affect the formation of molecular gas. And finally, the SF efficiency (SFE =SFR/M_{mol}, the inverse of τ_{dep}) depends on the physical properties of the molecular gas, such as the density and temperature of the giant molecular clouds (GMCs) and the fraction of diffuse molecular gas, not bound to GMCs.

Studies of large galaxy samples have demonstrated how the gas mass fraction (M_{gas}/M_*), the molecular gas mass fraction,

M_{mol}/M_*, and the molecular gas depletion time, τ_{dep}, depend on the position of the galaxy in the M_*- SFR plane. Scaling relations have been derived for local galaxies (e.g., Saintonge et al. 2011a,b, 2017; Janowiecki et al. 2020; Casasola et al. 2020) and for galaxies at high redshift (Genzel et al. 2015; Tacconi et al. 2018). Results show that τ_{dep} has only a weak dependence on stellar mass and on redshift, and it changes most significantly as a function of the distance to the SFMS ($\triangle$SFMS), with longer times below the SFMS. The total gas fraction M_{gas}/M_*, and molecular gas fraction, M_{mol}/M_*, decrease with stellar mass and also with $\triangle$SFMS. Together, these relations imply that a lack of gas is an important reason for the quenching of SF, but that changes in τ_{dep} also play a role.

In contrast to what one would expect, even at very high stellar masses, about 6% of galaxies have disks that have not quenched SF (Ogle et al. 2016, 2019b). Ogle et al. (2019b) selected a catalog of 84 super spirals (SSs) from the 1525 most optically luminous galaxies from the Sloan Digital Sky Survey. These spiral galaxies are extreme by many measures, with r-band luminosities of L = 8–14 L*, stellar masses of $M_* = 0.2$–1×10^{12} $M_\odot$, and giant isophotal diameters of $d_{25} = 55$–134 kpc. Their sSFR puts them on the SFMS. They have redshifts of 0.1 $< z < 0.3$ and appear uncommon in the local Universe. Progenitors for SSs have not yet been identified at much higher redshifts. Super spirals are very likely a remnant population of unquenched, massive disk galaxies. A large fraction (41%) have double nuclei, double disks or other signatures of ongoing mergers. Presently, their high mass protects their disks from destruction in a merger because the majority of super spiral mergers are now minor mergers (Ogle et al. 2019b). However, this leaves the open question of how SSs managed to become such massive disks in the first place. Possibly, super spirals have remained starforming disk galaxies compared to giant ellipticals because they reside in less massive dark halos than giant ellipticals of similar mass in stars. Alternatively, the super spirals with large bulge fractions may have formed more recently from a gas-rich spiral-elliptical minor merger (Jackson et al. 2022).

Super spirals are excellent objects to test galaxy evolution. Their extreme properties (size, stellar mass) provide a unique opportunity to extend studies of disk galaxy scaling laws to an entirely new regime, normally occupied by giant elliptical galaxies. In any case, the existence of super spirals demonstrates that the limit to spiral galaxy size and mass is much higher than previously thought, and that a high stellar mass can not be the primary cause of star-formation quenching. In fact, spiral galaxies with $M_* \sim 10^{11}$ $M_\odot$ may be most efficient at converting gas into stars, with mass fractions in stars approaching the cosmological baryon fraction (Posti et al. 2019; Di Teodoro et al. 2022).

In this paper, we present the first study of molecular gas in super spirals, derived from the CO(1-0) line intensity, for a sample of 46 super spirals and for a sample of 18 slightly less massive galaxies that are characterized by very broad atomic hydrogen (HI) emission lines. These data allow us to extend existing scaling relations to the mass regime of super spirals, find out how much molecular gas is available in these objects and whether the relation between molecular gas and SFR is comparable to less massive galaxies. This will give us insight into how SF proceeds in the most massive galaxies that have apparently escaped previous quenching mechanisms.

All rest-frame and derived quantities in this work assume a Kroupa (2001) initial mass function and a cosmology with $H_0 = 70$ km s^{-1} Mpc^{-1}, $\Omega_m = 0.7$, and $\Omega_\Lambda = 0.3$. The distance are derived from redshifts in the CMB-frame.

2. Sample and data

2.1. Samples

2.1.1. Sample of super spirals

We selected the sample of super spirals primarily from the catalogs of Ogle et al. (2016) and Ogle et al. (2019b). The galaxies in these catalogs were selected from the Sloan Digital Sky Survey (SDSS) from the r-band with $L_r > 8L^*$ and $z < 0.3$. In addition, following Ogle et al. (2019a), we selected additional objects from the 2 Micron All-sky Survey Extened Source Catalog (2MASX; Jarrett et al. 2000) which allowed us to include more edge-on, dusty galaxies. These latter objects were selected for $\log(M_*) > 11.6$ (estimated from the WISE band 1 luminosity and assuming a M/L ratio of 0.6), a slightly lower range in redshift of $z < 0.25$, and $d_{25} > 55$ kpc. From both samples, we selected galaxies with SFR > 10 $M_\odot$yr^{-1} (calculated from the WISE band 3 and 4 luminosities, following Cluver et al. 2014) in order to increase the probability of detection with the IRAM 30m Telescope. We selected in total 74 galaxies which were observed in CO(1-0) with the 30m telescope.

We then cleaned this sample by excluding 28 galaxies with a strong AGN, dominating the near-infrared and mid-infrared light and making the stellar mass and SFR determination uncertain (see Sect. 2.5.2). We present the molecular gas data for the AGNs, but we do not include the objects in the subsequent analysis. In this way, we end up with a sample of 46 star-forming super spiral galaxies. We call this sample the SS sample.

In addition, we included 18 slightly lower-mass ($\log(M_*) \gtrsim 11$ $M_\odot$) galaxies that have very broad HI-lines and high peak rotation speeds (> 300 km s^{-1}), indicating a large dynamical mass. These objects are more nearby than the super spiral sample (which are so rare that we do not find them in the local universe). We call this sample the "HI fast rotator" (HI-FR) sample. We include these objects because of the possibility to analyze also the HI content in a sample of galaxies with similar, albeit less extreme, properties as the super spirals, and because they fill the stellar mass gap between the SS and the comparison sample.

2.1.2. Comparison sample

Several catalogs of noninteracting, nearby galaxies containing CO, HI, SFR, and M_* exist in the literature; for example the AMIGA sample of isolated galaxies (Verdes-Montenegro et al. 2005; Lisenfeld et al. 2007, 2011), the xCOLDGASS sample of mass- selected nearby galaxies (Saintonge et al. 2011a,b, 2017), a catalogue of the ISM of normal galaxies (Bettoni et al. 2003), or an analysis of the scaling relations in DustPedia galaxies (Casasola et al. 2020). Here, we use the xCOLDGASS sample for comparison because it is a representative sample of nearby galaxies, and the CO observations have been taken with the IRAM 30m telescope and have been processed in a similar way as for our sample which makes the comparison more reliable[1]. The xCOLDGASS galaxy sample (Saintonge et al. 2017) is a mass-selected ($M_* > 10^9$ $M_\odot$) local sample of 532 nearby ($0.01 < z < 0.05$) galaxies. It was selected to be a representative sample for all galaxies in the SDSS survey, based on the distribution in the SFR-M_* plane. The HI fluxes were obtained from the xGASS survey (Catinella et al. 2018), a HI survey of 1179 observed with the Arecibo telescope.

---

[1] The data for this sample has been retrieved from http://www.star.ucl.ac.uk/xCOLDGASS/data.html

The angular size of the xCOLDGASS is small enough to fit almost completely inside the IRAM 30-m telescope beam width. A small aperture correction, f_{aper}, with a mean value of $f_{aper} \sim 1.17$, is applied in Saintonge et al. (2017) to the galaxies in xCOLDGASS in order to correct for the different fractions covered by the beam. For the aperture correction the procedure defined in Lisenfeld et al. (2011) was followed, which is also adopted in the present paper (Sect. 2.3.2) with a small difference in the choice of the assumed exponential scale length of the molecular gas distribution: For xCOLDGASS an exponential H_2 distribution with a scale length corresponding to the radius enclosing 50% of the SFn as measured in the SDSS/GALEX photometry was adopted (Saintonge et al. 2017). In the present paper, we also assume an exponential distribution of the H_2, but with exponential scale length $r_e = 0.2 \times r_{25}$ (see Sect. 2.3.2). We do not expect this relatively small difference to have any impact on our results, because the aperture corrections are small.

The molecular gas mass is calculated using a conversion factor α_{CO} that varies as a function of metallicity and distance to the SFMS, following Accurso et al. (2017). Given the large variety of properties in the xCOLDGASS sample, this is the best choice. A factor of 1.36 for He and heavy metals is taken into account as for our sample.

The SFR of the xCOLDGASS galaxies follows the prescription of Janowiecki et al. (2017) and is based for most galaxies on a combination of WISE band 4 (or band 3) and GALEX NUV luminosities. The calculation of both the stellar mass and the SFR are based on a Chabrier IMF (Chabrier 2003), which is very similar to the Kroupa IMF (Kroupa 2001) used in some of the prescriptions in the present paper.

2.2. Data

2.3. Molecular gas data

2.3.1. CO observations and data reduction with the IRAM 30m telescope

Observations were carried out between January and October 2020 with the Institut de Radioastronomie Milimetrique (IRAM) 30 m telescope on Pico Veleta within the projects 205-19 and 068-20. In addition, we retrieved data for one object (UGC 06066) from the IRAM archive. It had been observed in project 070-12 (PI. M. Haynes). We observed the redshifted $^{12}CO(1-0)$ in the central position of each galaxy. We used the dual polarization receiver EMIR in combination with the autocorrelator FTS at a frequency resolution of 0.195 MHz (corresponding to a velocity resolution of ~ 0.5 km s^{-1} at CO(1–0) at the frequency of our observations) and with the autocorrelator WILMA with a frequency resolution of 2MHz (corresponding to a velocity resolution of ~ 5 km s^{-1} at CO(1–0)). The observations were done in wobbler switching mode with a wobbler throw of 80″ in azimuthal direction. We confirmed for each galaxy that the off-position was well outside the galaxy.

The broad bandwidth of the receiver (16 GHz) and backends (8 GHz for the FTS and 4 GHz for WILMA) allow the observations of galaxies to be grouped into similar redshifts. The observed frequencies, taking into account the redshift of the objects, range between 89.6 GHz and 110.5 GHz. Each object was observed until it was detected with a S/N ratio of at least 5 or until a root-mean-square noise (rms) of ~ 1.5 mK (T_{mB}) was achieved for a velocity resolution of 20 km s^{-1} (only four objects were undetected with a higher rms between 1.6mK and 2.5 mK). The on-source integration times per object ranged between

20 minutes and 3 hours for most objects, and longer (6 hours) for UGC 06066. Pointing was monitored on nearby quasars every 60 – 90 minutes. During the observation period, the weather conditions were generally good, with a pointing accuracy better than 3-4 ″. Data taken in poorer conditions was rejected. The mean system temperature for the observations was 130 K for CO(1-0) on the T_A^* scale. At 100 GHz the IRAM forward efficiency, F_{eff}, is 0.95 and the beam efficiency, B_{eff}, is 0.79. The half-power beam size for CO(1-0) ranges between 22.5″ (for 110.5 GHz) and 27.6″ (for 89.6 GHz). All CO spectra and luminosities are presented on the main beam temperature scale (T_{mb}) which is defined as $T_{mb} = (F_{eff}/B_{eff}) \times T_A^*$.

The data were reduced in the standard way via the CLASS software in the GILDAS package[2]. We first discarded poor scans and data taken in poor weather conditions (e.g., with large pointing uncertainties) and then subtracted a constant or linear baseline. Some observations taken with the FTS backend were affected by platforming, that is the baseline level changed abruptly at one or two positions along the band. This effect could be reliably corrected because the baselines in between these (clearly visible) jumps were linear and could be subtracted from the different parts individually, using the *FtsPlatforming-Correction5.class* procedure provided by IRAM. We then averaged the spectra and smoothed them to resolutions of 10, 20 and 40 km s^{-1}.

We present the detected spectra in Appendix A. For each spectrum, we visually determined the zero-level line widths, if detected. The velocity-integrated spectra were calculated by summing the individual channels in between these limits. For nondetections we set an upper limit as

$$I_{CO} < 3 \times rms \times \sqrt{\delta V \, \Delta V}, \tag{1}$$

where δV is the channel width (in kilometers per second), ΔV the zero-level line width (in kilometer per second), and rms the root mean square noise (in Kelvin). For the nondetections, we assumed a line width of $\Delta V = 700$ km s^{-1} which is close to the mean velocity width found for CO(1-0) in the sample (mean $\Delta V = 708$ km s^{-1} with a standard deviation of 227 km s^{-1}). We considered spectra with a S/N ratio of the velocity integrated intensity > 5 as firm detections and those with a S/N rato in the range of 3-5 as tentative detections. The results of our CO(1-0) observations are listed in Table 1. We have 77 detections 42 SS, 15 HI-FR and 20 AGNs), 7 tentative detections (2 SS, 1 HI-FR and 4 AGNs) and 8 nondetections (2 SS, 2 HI-FR and 4 AGNs). In addition to the statistical error of the velocity-integrated line intensities, a calibration error of 15 % for CO(1-0) has to be taken into account (see Lisenfeld et al. 2019).

In addition to the central pointing, we mapped four objects (NGC 2713, NGC 5790, UGC 08902, and UGC 12591) at various positions along the major axis. The spacing between the pointings is 11″(about half the FWHM of the beam at 110 GHz) and the total number of pointings per galaxies ranged between 3 and 6. We show the individual spectra of the mapped galaxies in Appendix B.

2.3.2. Aperture correction

In most of our observations with the IRAM 30m telescope we only observed the galaxies in their central pointing. Since the galaxies in our sample are in general small, the central pointing covers a large fraction of the galaxy. However, this fraction

---

[2] http://www.iram.fr/IRAMFR/GILDAS

Table 1. Velocity-integrated CO intensities (central pointings)

Galaxy name	rms[a] [mK]	$I_{CO(1-0)}$[b] [K km s^{-1}]	det[c]	$\Delta V_{CO(1-0)}$[d] [km s^{-1}]
2MFGC12344	0.88	1.57 ± 0.13	0	1018
OGC 139	1.67	< 0.60	1	700
OGC 217	1.67	1.39 ± 0.14	0	347
OGC 290	1.46	1.02 ± 0.13	0	403
...	...	...	...	...

Notes. [a] Root-mean-square noise at a velocity resolution of 40 km s^{-1}. [b] Velocity integrated intensity and statistical error of the CO(1-0) line. [c] Detection code: 0 = detection (S/N $\gtrsim$ 5), 2 = tentative detection (S/N $\approx$ 3-5), 1 = nondetection. [d] Zero-level line width. The uncertainty is roughly given by the velocity resolution ($\sim$ 20 km s^{-1}). The full table is available online at the CDS.

Table 2. Extrapolated molecular gas mass

Galaxy name	z[a]	D_L[b] [Mpc]	log(M_{mol})[c] [$M_\odot$]	f_{aper}
2MFGC12344	0.141	665	10.58 ± 0.15	1.17
OGC 139	0.247	1244	< 10.66	1.15
OGC 217	0.249	1254	10.99 ± 0.16	1.05
OGC 290	0.296	1528	11.01 ± 0.17	1.05
...	...	...	...	...

Notes. [a] Redshift, z, from SDSS DR9 or DR13 (see Ogle et al. 2016, 2019a). [b] Luminosity distance, calculated adopting H$_0$ = 70 km s^{-1} Mpc^{-1}, Ω_m = 0.3 , Ω_Λ = 0.7. [c] Extrapolated molecular gas mass, except for UGC 12591 where the total mapped molecular gas mass is listed. The full table is available online at the CDS.

is different for each galaxy depending on its size. We therefore need to apply a correction for emission outside the beam. We carried out this aperture correction in the same way as described in Lisenfeld et al. (2011), assuming an exponential distribution of the CO flux:

$$S_{CO}(r) = S_{CO,center} \propto \exp(-r/r_e), \quad (2)$$

where $S_{CO,center}$ is the CO(1-0) flux in the central position derived from the measured I_{CO} applying the T_{mB}-to-flux conversion factor of the IRAM 30m telescope (5 Jy/K). Lisenfeld et al. (2011) adopted an exponential scale length of r_e = 0.2 × r_{25}, where r_{25} is the major optical isophotal radius at 25 mag arcsec^{-2}, from different studies of local spiral galaxies (Nishiyama et al. 2001; Regan et al. 2001; Leroy et al. 2008) and from their own CO data. Very similar values for r_e/r_{25} were found by Boselli et al. (2014) ($r_e/r_{25} \sim$ 0.2) and Casasola et al. (2017) (r_e/r_{25}= 0.17± 0.03) from an analysis of nearby mapped galaxies.

Thus, we adopt r_e = 0.2×r_{25} in eq. 2 and use this distribution to calculate the expected CO flux from the entire disk, $S_{CO,tot}$, taking the galaxy inclination into account, by 2D integration over the exponential galaxy disk (see Lisenfeld et al. 2011, for more details). Boselli et al. (2014) generalized this method to three dimensions by taking the finite thickness of galaxy disks into account. Except for edge-on galaxies ($i > 80°$) the 3D method gives basically the same result as the 2D approximation, and also for edge-on galaxies the difference is < 5% for z_{CO}/Θ < 0.1 (z_{CO} being the scale height of the CO perpendicular to the disk and Θ the beam size). We therefore consider the 2D aperture correction to be sufficient.

The resulting aperture correction factors, f_{aper}, defined as the ratio between $S_{CO,center}$ and the total aperture-corrected flux $S_{CO,tot}$, lie between 1.03 and 6.26 with a mean (median) value of 1.46 (1.13). There are 5 objects in the sample for which neither values for the inclination nor r_{25} were found. We adopted the median value of the sample, f_{aper}= 1.13, for them. The values of f_{aper} are listed in Table 2.

2.3.3. Molecular gas mass and α_{CO}

We calculated the molecular gas mass from the CO(1-0) luminosity, L'_{CO}, following Solomon et al. (1997) as:

$$L'_{CO}[\text{K km s}^{-1}\text{pc}^{-2}] = 3.25 \times 10^7 S_{CO,tot}\nu_{rest}^{-2}D_L^2(1+z)^{-1}, \quad (3)$$

where $S_{CO,tot}$ is the aperture-corrected CO line flux (in Jy km s^{-1}), D_L is the luminosity distance in Mpc, z the redshift, and ν_{rest} is the rest frequency of the line in gigahertz. We then calculated the molecular gas mass, M_{mol} (including a mass fraction of helium and heavy metals of a factor 1.36) as:

$$M_{mol}[M_\odot] = \alpha_{CO}L'_{CO}. \quad (4)$$

The conversion factor α_{CO} is known to vary as a function of metallicity. The most drastic variations occur in low-metallicty galaxies (12+log(O/H) $\lesssim$ 8.4), where α_{CO} increases steeply as a function of decreasing metallicity (see Bolatto et al. 2013). A considerably lower value of α_{CO} should be applied in starbursting galaxies lying well above ($\sim$ 1 dex) the SFMS. They are characterized by high surface densities which change the conditions of the ISM. In addition, Accurso et al. (2017) has shown that α_{CO} varies as a function of the distance to the MS for nonstarbursting galaxies, with higher values above the MS due to the stronger radiation field, and lower values below it. The effect produces a small correction of up to 12 % and should only be applied to nonstarbursting galaxies.

Based on the mass-metallicity relation, our SS+HI-FR sample is expected to have slightly super-solar metallicities. The difference is not expected to be very large because the metallicity approaches constant values for stellar masses above $\sim 10^{10.5} M_*$, independent of the exact method of measuring the metallicity (see Kewley & Ellison 2008; Mannucci et al. 2010). Adopting the prescription of Mannucci et al. (2010) (their eq. 2), we derive, based on the stellar mass and SFRs of the SS+HI-FR sample, a metallicity of 12+log(O/H) $\sim$ 9.0. With a solar metallicity of of 12+log(O/H) = 8.69 (Asplund et al. 2009) this gives a metallicities of a factor 2 higher than in the Solar neighborhood.

We use the metallicity dependence of α_{CO} from the prescription of Accurso et al. (2017) (their eq. 25) and of Bolatto et al. (2013) (their eq. 31) to predict the expected α_{CO} in SS+HI-FR galaxies. We ignore the dependence on the surface density included in the prescription of Bolatto et al. (2013) because SS+HI-FR galaxies are not in the starburst regime. We neither consider a possible dependence on the distance from the SFMS included in the prescription of Accurso et al. (2017) in order to keep the method simple and because the effect is small. We discuss the validity of our choice in Sect. 4.1. We predict α_{CO}= 2.95 from Accurso et al. (2017) (adopting 12+log(O/H) = 8.8 which is the maximum value for which their prescription is valid and which they recommend for higher metallicites) and α_{CO}= 3.5 from Bolatto et al. (2013). In addition, we take into account of

Table 3. Molecular gas mass from mapped objects

Galaxy name	$\left(\frac{r_{\text{map}}}{r_{25}}\right)^a$	$\log(M_{\text{mol,map}})^b$ [$M_\odot$]	$\left(\frac{M_{\text{mol,map}}}{M_{\text{mol}}}\right)^c$
NGC 2713	0.3	9.26	0.4
NGC 5790	0.6	9.53	0.6
UGC 08902	0.6	9.96	0.8
UGC 12591	1.0	9.55	1.1

Notes. [a] Ratio between maximum radial distance of the CO pointings to the radius of the galaxy at a surface brightness of 25 mag arcsec^2. [b] Decimal logarithm of the mapped molecular gas mass. [c] Ratio between mapped and extrapolated molecular gas mass.

the results of Wolfire et al. (2010) who calculated the fraction of dark gas, that is the fraction of molecular gas in a molecular cloud that does not contain CO, as a function of different parameters. They find (their Fig. 10) that this fraction decreases from roughly 30% (40%) for Solar metallicity and a mean surface density of 1.5×10^{22} cm^{-2} (0.75×10^{22} cm^{-2}) to value of 17% (25%) for a factor 1.9 higher metallicity. The decrease in dark mass fraction, f_{DG}, is thus a factor of 1.6 -1.8. This translates, adopting a simple picture in which $\alpha_{\text{CO}} \propto (1 - f_{\text{DG}})^{-1}$, to a value of α_{CO} between 3.5 - 3.6, in agreement with the relation of Bolatto et al. (2013).

Based on these predictions we adopt $\alpha_{\text{CO}} = 3$ $M_\odot$/(K km s^{-1} pc^{-2}) as a reasonable estimate for our galaxies, which is a factor 1.4 lower than the Galactic value ($\alpha_{\text{CO,Gal}} = 4.3$ $M_\odot$/(K km s^{-1} pc^{-2}, Bolatto et al. 2013). We note that this value is on the lower end of the range of α_{CO} predicted from the method considered above, which makes our derivation of M_{mol} conservative in the sense that we do not expect to overestimate M_{mol} with this choice of α_{CO}. Our adopted value of α_{CO} closely corresponds to what the Accurso et al. (2017) prescription would predict for galaxies of this mass and metallicity and is therefore consistent with the α_{CO} adopted for the comparison sample xCOLDGASS. The extrapolated molecular gas masses calculated with this conversion factor are listed in Tab. 2.

2.3.4. Mapped molecular gas mass

Four galaxies were mapped with 3-6 pointings along the major axis. For these, we derived the total flux from the average I_{CO} by applying an adjusted T_{mB}-to-flux conversion factor of 5 Jy/K $\times$ (mapped area/area of the CO(1-0) beam). Then, we calculated the total molecular mass from eq. 3 and eq. 4. In Table 3 the mapped molecular gas masses, $M_{\text{mol,map}}$, are listed and compared to the extrapolated values.

For all objects except UGC 12591, $M_{\text{mol,map}}$ is smaller than the extrapolated molecular gas mass which is not surprising because the mapping only covers part of the major axis (see column 2 in table 3). UGC 12591 was mapped furthest, out to r_{25}. Here, the mapped molecular gas mass is only slightly (10%) higher than the extrapolated value, showing that the extrapolation works well even for this relatively large object ($r_{25} = 45''$, $f_{\text{aper}} = 2.3$). For UGC 12591, we use the mapped molecular gas mass, $M_{\text{mol,map}}$, instead of the extrapolated value in the analysis of this paper.

2.4. Atomic gas mass

For the fast HI rotators, we obtained the velocity integrated HI fluxes, S_{HI}, from the Alfalfa survey (Haynes et al. 2018) and calculated the atomic gas mass as:

$$M_{\text{HI}} = \frac{2.36 \cdot 10^5}{(1 + z)^2} \cdot \left(\frac{S_{\text{HI}}}{\text{Jy km s}^{-1}}\right)\left(\frac{D_{\text{L}}}{\text{Mpc}}\right)^2, \qquad (5)$$

(see Meyer et al. 2017; Saintonge & Catinella 2022). No correction for Helium and metals is included. For UGC 12521 the value from di Teodoro et al. (2022) (their Tab. 1), adapted to our distance and no Helium, is used.

2.5. WISE data

2.5.1. WISE photometry

WISE galaxy measurements come from the WISE Extended Source Catalog (WXSC; Jarrett et al. 2013, 2019). It utilizes custom image mosaic construction of the four WISE bands: 3.4, 4.6, 12, and 23 μm (Jarrett et al. 2012) which preserves native resolution. It catalogues complete resolved source characterization that includes careful contaminant removal, local background estimation, size and orientation, a suite of photometric, surface brightness, and radial profile measurements (see Jarrett et al. 2013, 2019).

Based on these maps we estimated total fluxes by modeling the emission profile in each band, constructing axi-symmetric radial profiles, which were fitted with a double-Sersic function to represent the spheroidal and disk population distributions, extrapolated to several disk scale lengths to determine the total emission.

We then derived rest-frame fluxes using SED modeling of the observed-frame fluxes. As described in Jarrett et al. (2019, 2023), a suite of composite templates (ranging across all morphological types) are (1+z) scaled to the redshift of the object and fit to the measurements. The best match is then used to provide observed-to-rest flux corrections. Errors in the corrections are driven by the photometric quality, number of available measurements to define the SED, and the finite set of templates. Based on the analysis in Yao et al. (2022), the k-correction imparts less than 5-10% uncertainty for most sources that have redshifts < 0.3 (see the Appendix in Yao et al. 2022).

In Tab. 4 we list the total measured, and the k-corrected fluxes in the four WISE bands.

2.5.2. Determination of AGN activity from WISE colors

WXSC mid-IR colors can be used to separate quiescent, actively SF or AGN dominated galaxies. We use the W1-W2 and W2-W3 colours and the classification of Jarrett et al. (2017), as presented in Jarrett et al. (2019, their Fig. 10), to separate galaxies with dominant AGN emission in the mid-IR (Fig. 1). We use the prescription from Jarrett et al. (2019, their eq. 1) to define the mid-IR star-forming sequence:

$$[W1 - W2] = 0.015 \times \exp([W2 - W3]/1.38) - 0.08 \qquad (6)$$

and define galaxies as AGN dominated if they lie above the "warm AGN" line in Fig. 1 which is offset by +0.3 mag from the mid-IR star-forming sequence. We exclude AGN dominated objects from our analysis because we cannot derive reliable values

Table 4. WISE fluxes and classification

Galaxy name	$F_{W1,obs}{}^a$ [mJy]	$F_{W1,kcorr}{}^b$ [mJy]	$F_{W2,obs}{}^a$ [mJy]	$F_{W2,kcorr}{}^b$ [mJy]	$F_{W3,obs}{}^a$ [mJy]	$F_{W3,kcorr}{}^b$ [mJy]	$F_{W4,obs}{}^a$ [mJy]	$F_{W4,kcorr}{}^b$ [mJy]	Type^c
2MFGC12344	3.14 ± 0.10	4.56 ± 0.05	1.81 ± 0.09	2.75 ± 0.03	3.24 ± 0.60	4.17 ± 0.19	5.52 ± 0.99	5.54 ± 0.89	SS
OGC 139	0.90 ± 0.04	1.68 ± 0.02	0.57 ± 0.04	1.27 ± 0.02	1.47 ± 0.12	2.65 ± 0.10	2.20 ± 0.80	2.65 ± 0.59	SS
OGC 217	0.72 ± 0.03	1.23 ± 0.02	0.51 ± 0.04	1.10 ± 0.02	4.23 ± 0.23	5.26 ± 0.16	14.19 ± 1.20	6.67 ± 0.69	SS
OGC 290	0.59 ± 0.03	1.20 ± 0.02	0.41 ± 0.03	1.07 ± 0.01	2.28 ± 0.20	3.04 ± 0.15	6.77 ± 1.13	3.43 ± 0.57	SS
...	...	...	...	...	...	...	...	...	...

Notes. $^{(a)}$ Photometrically measured fluxes and photometrical error. $^{(b)}$ Fluxes with applied k-corrections (as described in Sec. 2.5). $^{(c)}$ Galaxy type (SS= super spiral, HI = HI fast rotator, AGN = AGN dominated galaxy). The distinction between AGN and SF galaxies (i.e, SS+HI-FR) was done based on the WISE colours as described in Sect. 2.5.2. Fluxes with a signal-to-noise ratio < 3 are considered upper limits in the analysis. The full table is available online at the CDS.
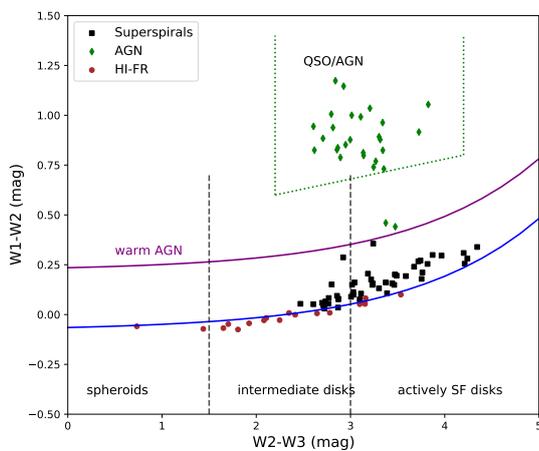
Fig. 1. WISE color magnitude plot for the SS, HI fast rotator and AGN galaxies, following the classification scheme of Jarrett et al. 2019 (their Fig. 10). The green dotted lines indicate the zone populated by QSO/AGN, following Jarrett et al. (2011). The blue line gives the sequence of SF galaxies (eq. 1 from Jarrett et al. 2019), from quiescent objects (low [W2-W3]) to actively star-forming objects (high [W2-W3]). The purple line, labeled "warm AGN", indicates the region where low-level Seyferts and Liners reside (see Jarrett et al. 2011). We adopt this as the dividing line between star-forming and AGN dominated galaxies and flag galaxies above this line as AGN-dominated.

for the SFR and the stellar mass since the mid-IR luminosities are to a large extent due to AGN and not stellar emission. Based on this criterion, 28 galaxies are AGN dominated. In Tab. 4 the resulting classification codes are listed.

2.6. GALEX data

Near-ultraviolet (NUV) images from the Galaxy Evolution Explorer (GALEX) satellite were extracted from the Mikulski Archive for Space Telescopes (MAST) GALEX GR6/7 archive[3] for the 55 SS+HI-FR sample. Nine galaxies did not match any GALEX observation because some regions of the sky were not observed due to either bright UV source avoidance or because of very high stellar density close to the plane of the Milky Way. In some cases, several different images contained the same target

object. In such cases we used the image with the longest integration time for our analysis.

NUV emission was extracted from the GALEX science images in counts s^{-1} over a circular aperture corresponding to the isophotal diameter D_{25} obtained from the NASA Extragalactic Database (NED; D_{25} is the B-band isophotal diameter at a surface brightness of 25 mag arcsec^2). Background subtraction was achieved by subtracting the counts s^{-1} in the background image evaluated over the same area. Surface brightness profiles were also extracted to ensure that D_{25} was a good representation of the main body of UV emission for each object. In almost all cases, a large fraction of the UV light was captured inside this diameter. Each image was visually inspected to ensure that there were no bright contaminating stars within the aperture. Only in two cases were bright stars found near the edge of the aperture, and these were masked to preserve the quality of the photometry. Uncertainties in the measured fluxes were evaluated by adding both shot noise and background uncertainty together in quadrature. Background uncertainties were difficult to measure directly from the images, often leading to unrealistically small values, and so we assumed a conservative average background uncertainty of 2% (and 5% for FUV) based on documentation provided by GALEX home page. In addition, a calibration error of 14.8% (Gil de Paz et al. 2007) has to be added in quadrature.

Conversion from count s^{-1}, c, to AB magnitde, $M(AB)_{NUV}$ followed the standard relation given in the GALEX User Manual $M(AB)_{nuv} = -2.5 \times \log_{10}(c) + 20.08$. These photometric magnitudes were corrected for Galactic extinction assuming a value for E(B-V) determined from Schlegel et al. (1998) with the additional recalibration corrections of Schlafly & Finkbeiner (2011). Following Bianchi (2011) we assumed a Galactic extinction curve and $A_{NUV}/E(B-V) = (R_{NUV} = 7.95)$. The measured fluxes, together with their photometrical errors, are listed in Tab. 5.

We also applied a k-correction following Chilingarian et al. (2010); Chilingarian & Zolotukhin (2012)[4]. The k-correcting was small, less than 10% for 47 objects, and between 10% and 25% for the remaining eight objects.

2.7. Star formation rate and stellar mass

For both the calculation of the SFR and the stellar mass different prescriptions exist in the literature. Normally, the stellar mass is derived from the near-infrared emission and the SFR can be derived from the ultraviolet (UV), combined with the mid-infrared (to probe dust-enshrouded SF).

---

[3] see http://galex.stsci.edu/GR6/

[4] We used the online-calculator at http://kcor.sai.msu.ru/

Table 5. Measured GALEX NUV flux and photometric error, SFR and M_*.

Galaxy name	$F_{\rm NUV}$ [μJy]	log(SFR) [$M_\odot$ yr^{-1}]	log(M_*) $M_\odot$
2MFGC12344	58.0 ± 1.4	0.99	11.65
OGC 139	38.2 ± 0.9	1.14	11.65
OGC 217	66.7 ± 4.6	1.89	11.56
OGC 290	64.2 ± 1.8	1.78	11.65
...	...	...	...

Notes. SFR and M_* calculated as described in Sect. 2.7. The full table is available online at the CDS.

In the present work, we therefore tested and compared different methods (see Appendix C and D) to ensure that the used prescription gives consistent results for the SS+HI-FR and the comparison sample which cover different stellar mass ranges. None of the existing SFR or M_* prescriptions has been tested so far in the high stellar mass range of super spirals. As shown by Leroy et al. (2019), the coefficients of the prescriptions have a dependence on stellar mass, and therefore we need to test as well as possible that the existing methods hold for higher masses. Apart from comparing different prescriptions, we also compare them to SED fitting with CIGALE (Boquien et al. 2019) in order to derive both the SFR and the stellar mass in an independent way (Appendix E).

2.7.1. Star formation rate

In the present paper, we calculate the SFR from GALEX and WISE data, in order to probe both dust-free and dust-enshrouded SF. It is important to use the same method for all samples of our study. We decided to follow the method used in xCOLDGASS to calculate their SFR$_{\rm best}$ parameter (Saintonge et al. 2017). SFR$_{\rm best}$ was calculated following a "SFR ladder" (see Janowiecki et al. 2017). A combination of GALEX NUV and WISE luminosities was used (preferentially W4, and, if not detected, W3) for all galaxies with good WISE and GALEX data, and for the remaining cases (30% of the galaxies) the SFR was derived from SED fitting.

We use a very similar prescription for the SS+HI-FR galaxies. We calculate the SFR from W4+NUV (eq. 3 Janowiecki et al. 2017) for those galaxies with good (S/N > 3) data for both the NUV and W4 bands (42 galaxies). For galaxies with good NUV data but poor W4 data, we use eq. 4 of Janowiecki et al. (2017) and calculate the SFR from W3+NUV (13 galaxies). For the remaining 8 galaxies with neither good W4 data nor good or existing NUV data we calculate the SFR only from W3 data alone. Here, we use the prescription by Cluver et al. (2017) (their eq. 4), lowered by a 0.2 dex in order to guarantee a consistent normalization (see Appendix D). Thus, we use the following formulae for the SFR (in order of decreasing preference):

$$SFR_{W4+NUV,J17}[{\rm M_\odot yr^{-1}}] = L_{\rm NUV} 10^{-43.29} + L_{\rm W4,dust} 10^{-42.70} \quad (7)$$

$$SFR_{W3+NUV,J17}[{\rm M_\odot yr^{-1}}] = L_{\rm NUV} 10^{-43.29} + L_{\rm W3,dust} 10^{-42.89} \quad (8)$$

$$SFR_{W3,C17}[{\rm M_\odot yr^{-1}}] = 0.889 L_{\rm W3,dust} 10^{-42.89} 10^{-41.54} \quad (9)$$

where $L_{\rm NUV}$ is the luminosity of the GALEX NUV band and $L_{\rm W3,dust}$, $L_{\rm W4,dust}$ are the luminosities from the dust contribution to the WISE W3 and W4 bands. The latter are obtained from the total luminosities in these bands after subtracting the stellar continuum based on the W1 luminosity, $L_{\rm W1}$, calculated following Jarrett et al. (2011) as in Cluver et al. (2017) as $L_{\rm W3,dust} = 0.158 \times L_{\rm W1}$ and $L_{\rm W4,dust} = 0.059 \times L_{\rm W1}$ (very similar to the coefficients of Janowiecki ($L_{\rm W3,dust,J17} = 0.201 \times L_{\rm W1}$, and $L_{\rm W4,dust,J17} = 0.044 \times L_{\rm W1}$). All luminosities are defined as νL_ν and are in units of erg s^{-1}.

As shown in Appendix E, this definition of the SFR agrees well with the results from CIGALE for the SS+HI-FR sample. In Appendix D, we compare our prescriptions for both xCOLDGASS and SS+HI-FR with the prescriptions of Leroy et al. (2019) and Cluver et al. (2017) and find in general good correlations, (albeit with a constant offset in the case of Cluver et al. 2017)). From this comparison we conclude that the systematic uncertainty in the SFR is about 0.2 dex.

2.7.2. Stellar mass

The stellar mass can be well traced by the mid-infrared emission and it is frequently derived from the WISE 3.4 μm (W1) luminosity. For this, a stellar mass-to-light ratio, $\Upsilon_*^{3.4}$ (in units $M_\odot/L_{\rm W1,\odot}$)[5] has to be adopted, which depends, however, considerably on the properties of a galaxy, in particular the age of the stellar population. Typical values range between $\Upsilon_*^{3.4} \approx 0.1-0.7$ $M_\odot/L_{\rm W1,\odot}$ (e.g., Leroy et al. 2019). There are different prescriptions to calculate the stellar mass from the mid-infrared luminosities. Some use simply a constant mass-to-light ratio $\Upsilon_*^{3.4}$ (e.g., Eskew et al. 2012), whereas other use values of $\Upsilon_*^{3.4}$ that depend on mid-IR color (e.g., Jarrett et al. 2013; Cluver et al. 2014; Jarrett et al. 2023), or sSFR (Leroy et al. 2019).

All these prescriptions have not been tested in the mass range of super spiral galaxies. Therefore, in Appendix D, we compare different prescription for the xCOLDGASS and the super spiral sample, and in Appendix E we compared the prescriptions to CIGALE. For the SS+HI-FR sample, we find a good correlation of the stellar mass derived from CIGALE and those derived with $\Upsilon_*^{3.4} = 0.5$. There is also a good correlation of the CIGALE results with the stellar mass of Leroy et al. (2019), albeit with a small offset of 0.1 dex. Considering the uncertainties and in order to keep the derivation of the stellar mass simple, we use a constant $\Upsilon_*^{3.4} = 0.5$ for our SS+HI-FR sample. For the xCOLDGASS sample, mostly for consistency with other studies, we use the stellar mass provided in Saintonge et al. (2017) which was taken from the SDSS DR7 MPIA-JHU catalog. Good correlations with the prescription of Leroy et al. (2019) and with Cluver et al. (2014) exist (for the latter with a constant offset of 0.3 dex).

3. Results

The goal of this study is to compare the molecular gas mass, stellar mass and SFR of very massive, star-forming galaxies to those of galaxies with lower stellar masses. In order to properly compare our SS+HI-FR sample to the comparison sample, we need to (i) take into account that the SS galaxies are further away than the HI-FR and xCOLDGASS galaxies. Both the molecular gas fraction ($f_{\rm mol}= M_{\rm mol}/M_*$) and the sSFR have a strong dependence on redshift z (e.g., Genzel et al. 2015; Tacconi et al. 2018) and

---

[5] We use, as Leroy et al. (2019) and Cluver et al. (2014), a value of $L_{\rm W1,\odot} = 1.6 \times 10^{32}$erg^{-1}

we need to correct for this trend in order to carry out a meaningful comparison. (ii) Many properties of a galaxy depend very sensitively on the distance to the SFMS. We subsequently analyse our results with respect to this parameter. There are different prescriptions for the SFMS in the literature, mostly due to differences in the way how to calculate the SFR, and also due to details of the sample selection. We adopt the prescription of Janowiecki et al. (2020) which was derived from the xCOLDGASS sample.

3.1. Redshift-dependence of sSFR and M_{mol}/M_*

Both the sSFR and the molecular gas mass fraction (M_{mol}/M_*) are known to have a strong dependence on the redshift. This can be clearly seen for galaxies in the SS sample (Figs. 2 and Fig. 3, upper panels). We need to correct for this redshift dependence in order to compare the SS sample to the $z \approx 0$ (HI-FR and xCOLDGASS).

Speagle et al. (2014) studied the SFMS of galaxies at different redshifts and derived a prescription for the SFMS as a function of z (sSFR$_{MS,S14}(M_*, z)$). We adopt this prescription (as cited in Tacconi et al. 2018, their eq. 1)) to derive a sSFR reprojected to $z = 0$ for the SS, by applying sSFR$_{zcorr}$ = sSFR $\cdot$ (sSFR$_{SFMS,S14}(M_*, z = 0)$/sSFR$_{SFMS,S14}(M_*, z)$). In a similar way, we reproject the molecular gas fraction of the SS galaxies to $z = 0$, by applying the nonlinear relation of Tacconi et al. (2020, from their Tab. 3, see also their Fig. 5) which is, due to the curved shape of the z-dependence, more appropriate for low z galaxies than the general linear relation $f_{mol} \propto (1 + z)^{-2.5}$ (Tacconi et al. 2018). We thus correct the molecular gas fraction as $f_{mol,zcorr} = f_{mol} + 3.62 \cdot (0.66^2 - (\log(1+z) + 0.66)^2)$. In the following analysis, we always use the redshift-corrected values of the sSFR and the molecular gas mass fraction, except for the calculation of the depletion time which is based on observed values of SFR and M_{mol}.

In Figs. 2 and Fig. 3 (lower panels) we show the corresponding relations for the z-corrected quantities. The applied correction eliminate the trends of both sSFR and f_{mol} with z to a large extent, although a weak relation with redshift is still visible (a linear least-square fit yields sSFR$_{zcorr} \propto (1 + z)^{1.4}$ and $f_{mol,zcorr} \propto (1 + z)^{0.84}$).

Fig. 4 shows the relation of the stellar mass with redshift. There is only a weak trend with redshfit ($M_* \propto (1 + z)^{1.16}$), showing that in our sample there is a weak tendency for the more massive galaxies to be more distant.

3.2. Star-forming main sequence

Figure 5 shows the relation between the SFR and stellar mass. The properties of a galaxy are determined to a large extent from its position in this plane, and in particular whether the galaxy lies on, above or below the SFMS. We include the SFMS together with its width, defined as the 1σ scatter, derived for the xCOLDGASS sample by Janowiecki et al. (2020, their equations 1 and 2). This relation is practically identical to that derived by Leroy et al. (2019) for a sample of 15000 nearby galaxies. Following Janowiecki et al. (2020), we split the sample into "starburst" objects (> 0.3 dex above the SFMS), SFMS objects (within ± 0.3 dex of the MS) and quiescent objects (more than 0.3 dex below the SFMS). Janowiecki et al. (2020) distinguished within this quiescent subsample furthermore between transitioning objects (between 0.3 dex and 1.55 dex below the MS) and red-sequences objects (more than 1.55 dex below the MS). We
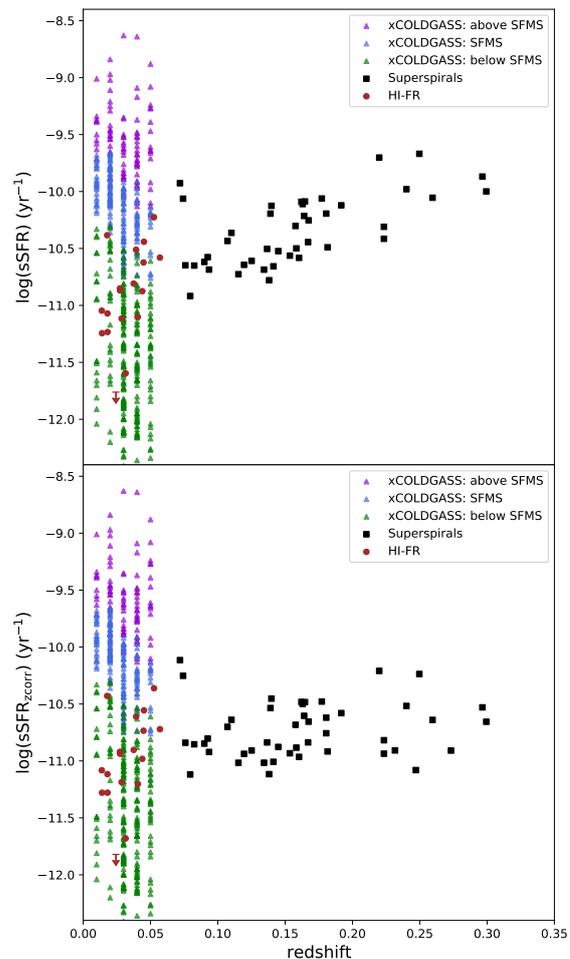
Fig. 2. Redshift dependence of the sSFR. *Upper panel:* Specific SFR as a function of redshift for the SS, HI-FR and the xCOLDGASS sample. *Lower panel:* The specific SFR for the SS has been adjusted to $z = 0$ following the z-dependence of the SFMS by Speagle et al. (2014). sSFR for xCOLDGASS and HI-FR are the same as in the upper panel.

do not include the latter distinction, because none of our SS+HI-FR objects lies in the quiescent regime.

Figure 5 shows that the SSs follow very well the extrapolation of the SFMS derived by Janowieski, with practically all objects lying within the 1 σ width. This means that in spite of their large mass, SSs are forming stars at a rate which puts them on the same SF relation as lower-mass spirals. On the other hand, the sample of fast HI rotators contains galaxies which lie on the SFMS and galaxies which are well below, in the range of transitioning galaxies.

In the following, when appropriate, we distinguish between star-forming and transitioning HI-FR galaxies as those that are on the SFMS (within± 0.3 dex) or more than 0.3 dex below the SFMS. With respect to the SS galaxies, we consider them all as belonging to the MS. In addition, we define the distance to the

Table 6. Mean value, its error, and median value for the SS and HI-FR sample. Upper limits are treated as detections.

	SS (n = 46)		FR-HI (SFMS) (n= 6)		FR-HI (below SFMS) (n= 12)		xCOLDGASS (SFMS)[b]	
	mean (err)	median	mean (err)	median	mean (err)	median	mean (err)	median
$\log(\mathrm{sSFR})_{\mathrm{zcorr}}$ (yr^{-1})	-10.73 (0.04)	-10.81	-10.57 (0.04)	-10.59	-11.20 (0.06)	-11.15	–	–
$\log(f_{\mathrm{mol,zcorr}})$	-1.39 (0.02)	-1.38	-1.27 (0.04)	-1.28	-1.87 (0.09)	-1.83	–	–
τ_{dep}(yr)	9.29 (0.03)	9.33	9.28 (0.04)	9.27	9.32 (0.06)	9.30	8.98 (0.02)	9.00
$\tau_{\mathrm{dep}}(\mathrm{SFR}_{\mathrm{C17}})^a$ (yr)	9.32 (0.02)	9.33	9.27 (0.02)	9.28	9.26 (0.15)	9.26	8.90 (0.02)	8.87
$\mu_* \ M_\odot$ kpc^{-2}	8.69 (0.04)	8.68	8.93(0.15)	8.85	9.06(0.06)	9.09	8.42 (0.05)	8.45
$\log(f_{\mathrm{HI}})$	–	–	-0.78 (0.09)	-0.86	-1.00 (0.11)	-0.99	–	–
$\log(M_{\mathrm{mol}}/M_{\mathrm{HI}})$	–	–	-0.40 (0.11)	-0.27	-0.82 (0.11)	-0.79	-0.48 (0.05)	-0.48

Notes. [a] Gas depletion time calculated with the prescription of Cluver et al. (2017), shifted by +0.2 dex. [b] Values are only given for quantities that have a weak dependence on M_*.

SFMS as $\triangle$(SFMS) = $\log$(sSFR)(yr^{-1}) $-\log$(sSFR$_{\mathrm{MS,Jan20}}$)(yr^{-1}), where sSFR$_{\mathrm{MS,Jan20}}$ is the SFMS from Janowiecki et al. (2020). In Tab. 6 the mean and median values, as well as the standard deviation for the sSFR of the SS and HI-FR samples are given.

3.3. Molecular gas mass fraction

Figure 6 shows the scaling relation between the molecular gas fraction M_{mol}/M_* and the stellar mass. Included is, as a yellow line, the scaling relation found by Janowiecki et al. (2020) for the xCOLDGASS sample, (which they called the H$_2$ main sequence, H$_2$MS) and its 0.2 dex widths which was derived as the standard deviation of the SFMS galaxies in this relation.

The molecular gas fractions of SS galaxies lie mostly above the scaling relation found for lower-mass SFMS galaxies (the mean value of $f_{\mathrm{mol,zcorr}}$ of SS, see Tab. 6 is roughly 0.2 dex above the value of the H$_2$MS at the stellar mass of SS). This means that SS galaxies have a large reservoir of molecular gas, higher than what is expected for SFMS galaxies of their mass, if one extrapolated from lower masses. FR-HI galaxies that lie on the SFMS, also have a relatively high molecular gas mass fractions, lying in the upper half of the H$_2$MS, whereas FR-HI galaxies below the SFMS also have molecular gas fractions below the H$_2$MS .

Fig. 7 displays the molecular gas mass fraction as a function of the distance to the SFMS. Here, SS and HI-FR galaxies follow the same trend as galaxies from the comparison sample. This means that SS+HI-FR galaxies have the molecular gas fraction that corresponds to their SF activity. Taken together, these two relations suggest that the decrease of $f_{\mathrm{mol,zcorr}}$ with stellar mass for star-forming disk galaxies is less than what is suggested from the extrapolation of the H$_2$MS relation from lower-mass galaxies. In other words, $f_{\mathrm{mol,zcorr}}$ for the highest stellar masses seems to be biased low when only considering the xCOLDGASS data. If we include the SS+HI-FR galaxies together with the xCOLDGASS sample and again fit the relation (considering only galaxies on the SFMS) we derive $f_{\mathrm{mol,zcorr}}$ = (-0.18 ± 0.02) × ($\log(M_*)$-9) - (0.95± 0.4), slightly flatter than the relation in Janowiecki et al. (2020) ($f_{\mathrm{mol,zcorr}}$= (-0.26 ± 0.03) × ($\log(M_*)$-9) - (0.90± 0.18)).

3.4. Molecular gas depletion time

Figure 8 shows the depletion time, $\tau_{\mathrm{dep}}= M_{\mathrm{mol}}$/SFR, as a function of stellar mass. Here, neither the SFR nor the molecular gas mass are corrected for redshift.

The SS and HI-FR galaxies have longer gas depletion times (mean value $\log(\tau_{\mathrm{dep}}) \sim 9.3$ yr , see Tab. 6) than the comparison sample (mean $\log(\tau_{\mathrm{dep}})$ of xCOLDGASS for galaxies on the SFMS is 9.0 yr). In general, only a weak trend of τ_{dep} with M_* has been found in the literature, both for nearby galaxies (Saintonge et al. 2017) and at higher redshifts, up to $z = 4$ (Genzel et al. 2015; Tacconi et al. 2018). We include in Fig. 8 as a yellow line a relation of $\log(\tau_{\mathrm{dep}}) \propto M_*^{0.203}$ from (Saintonge & Catinella 2022, their Fig. 8), which fits the trend in all the samples reasonably well. The long depletion time of the SS+HI-FR sample might thus be the continuation of a trend with stellar mass that is also seen in the xCOLDGASS galaxies above a mass of about $\log(M_*) \sim 10.5$. In Fig. 9 we show τ_{dep} as a function of the distance to the SFMS. In studies of close-by galaxies (Saintonge et al. 2017; Janowiecki et al. 2020) and high-z galaxies (Tacconi et al. 2018) the depletion time has been found to depend on the distance to the SFMS, with quiescent galaxies having considerably higher values for τ_{dep}. We include in the figure the relation found by Tacconi et al. 2018 ($\tau_{\mathrm{dep}} \propto \triangle$(SFMS)$^{-0.44}$). The relation fits very well the xCOLDGASS galaxies, but the SS+HI-FR galaxies lie considerably above it, showing that they have a rather long depletion time for their position on the SFMS.

Finally, Fig. 10 shows τ_{dep} as a function of redshift. As expected, only a weak trend is visible. Genzel et al. (2015) and Tacconi et al. (2018) found that τ_{dep} decreases with redshift ($\tau_{\mathrm{dep}} \propto (1+z)^{-0.6}$, Tacconi et al. 2018) which we include for illustration in the plot (yellow line), together with the best-fit relation to the data ($\tau_{\mathrm{dep}} \propto (1 + z)^{-0.02}$). Within the redshift range covered by the SS sample, the effect of this weak relation is small with a difference in τ_{dep} of < 0.1 dex. There is a clear offset between the SS+HI-FR sample and the xCOLDGASS sample even for low redshifts. We conclude, therefore, that the difference in τ_{dep} between xCOLDGASS and SS+HI-FR is not due to redshift, but rather due to intrinsic properties of the galaxies. We further discuss this in Sect 4.

3.5. Atomic and molecular gas in HI fast rotators

Figure 11 shows the properties of the atomic gas in the HI-FR galaxies. Due to their higher redshift, no HI data exists for
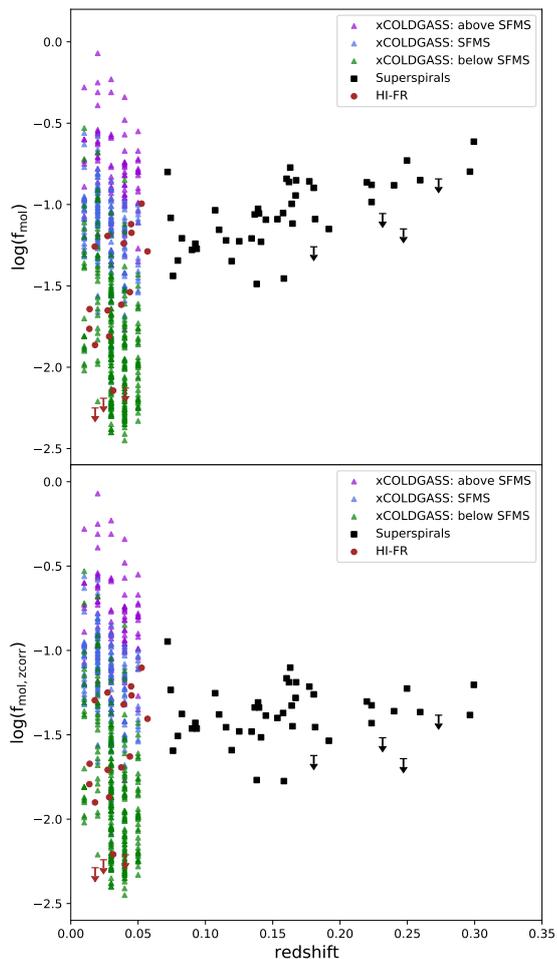
Fig. 3. Redshift dependence of the molecular gas fraction. *Upper panel:* The molecular gas fraction f_{mol} (= M_{mol}/M_*) as a function of redshift for the SS, HI-FR galaxies and the xCOLDGASS sample (only detections in CO for xCOLDGASS in order not to overload the figure). *Lower panel:* The molecular gas fraction f_{mol} for the SSs has been adjusted to $z = 0$ following the nonlinear z-dependence found by Tacconi et al. (2020, their Tab. 3). f_{mol} for xCOLDGASS and HI-FR are the same as in the upper panel.

SS galaxies. In the upper panel we show the atomic gas fraction, f_{HI} = M_{HI}/M_*, together with the scaling relation found by Janowiecki et al. (2020) for xCOLDGASS galaxies. The atomic gas fraction of HI-FR objects lies clearly above the relation found for lower-mass galaxies, both for SFMS and for below-SFMS objects (see Tab. 6), which can be explained by the selection of the sample. Detected galaxies from the ALFALFA survey tend to be HI bright, and in addition we selected galaxies with very broad HI spectra.

The molecular-to-atomic gas fraction for galaxies on the SFMS, on the other hand, is similar to xCOLDGASS. Together with the relations found for the molecular gas in Sect. 3.3, this shows that actively star-forming HI-FR objects are in general
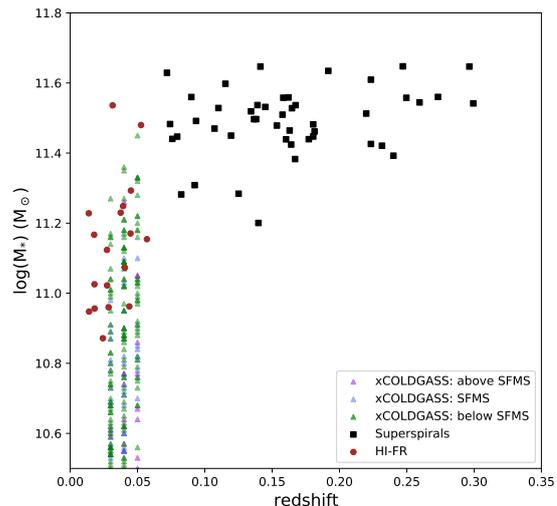
Fig. 4. M_* as a function of redshift for the super spirals, HI-FR galaxies and the xCOLDGASS sample. Only a weak trend of M_* with redshift is visible ($M_* \propto (1 + z)^{1.16}$).
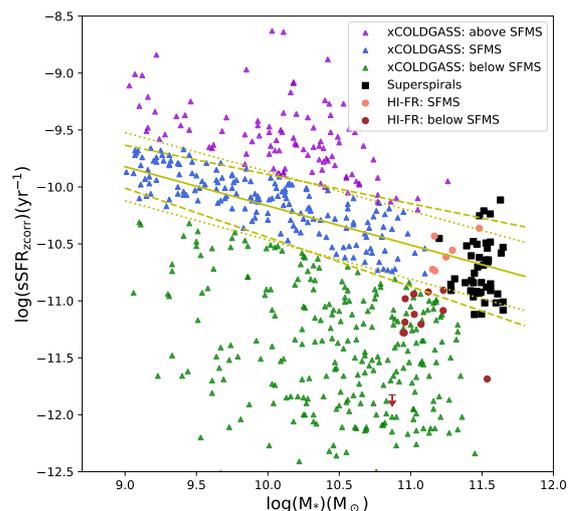
Fig. 5. sSFR as a function of stellar mass for the SS, HI-FR and the xCOLDGASS sample. The sSFR of the SS galaxies is adjusted to $z = 0$ according Speagle et al. (2014) as explained in Sect. 3.1. The full yellow line denotes the SFMS from Janowiecki et al. (2020), derived for the xCOLDGASS sample, and the dashed yellow line shows its 1σ scatter. The dotted yellow line show a distance of 0.3 dex from the SFMS which is adopted, following Janowiecki et al. (2020), to define SFMS galaxies.

gas-rich, both for atomic and for molecular gas. The transformation from atomic to molecular gas seems to be similar as in lower-mass galaxies.

4. Discussion

The major findings of our analysis are: (i) In agreement with the earlier results of Ogle et al. (2019a), super spiral galaxies
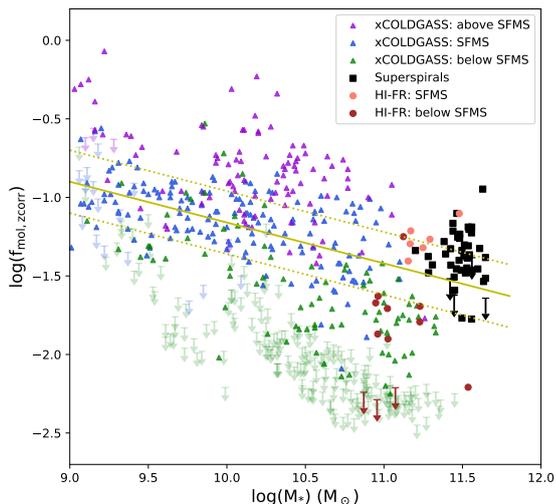
Fig. 6. Molecular gas mass fraction ($f_{mol,zcorr}$), as a function of stellar mass for the super spirals, HI-FR and the xCOLDGASS sample. The molecular gas mass of the SS galaxies is reprojected to $z = 0$ following Tacconi et al. (2018) as explained in Sect. 3.1.
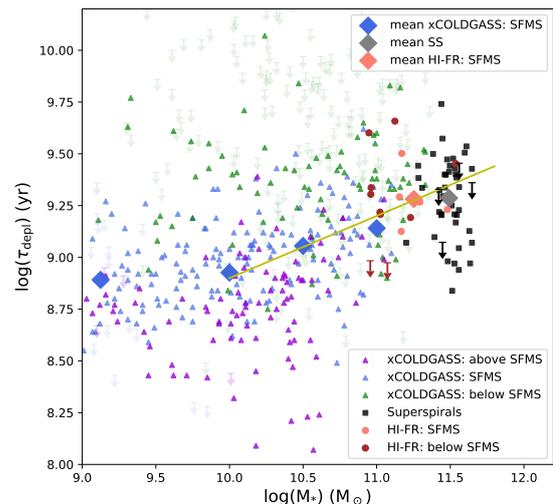

Fig. 8. Gas depletion time $\tau_{dep} = M_{mol}/$SFR as a function of stellar mass for the SS, HI-FR and the xCOLDGASS sample. The yellow line gives, for illustration, the relation from Saintonge & Catinella (2022, their Fig. 8, $\log(\tau_{dep}) = 0.203 \log(M_*) + 6.79$).
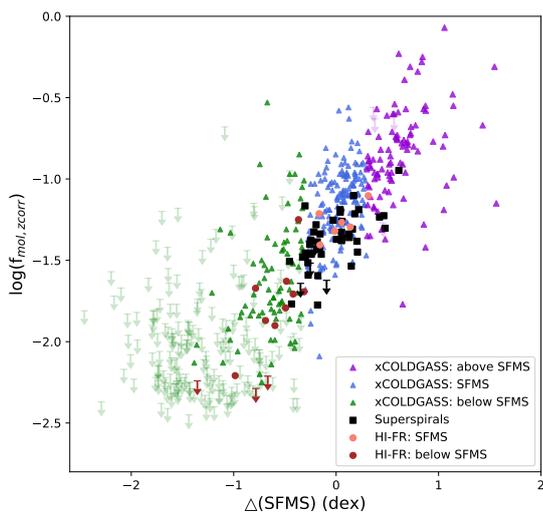
Fig. 7. Molecular gas mass fraction ($f_{mol,zcorr}$), as a function of distance to the SFMS for the SS, HI-FR and the xCOLDGASS sample. The molecular gas mass of the SS galaxies is reprojected to $z = 0$ following Tacconi et al. (2018) as explained in Sect. 3.1.
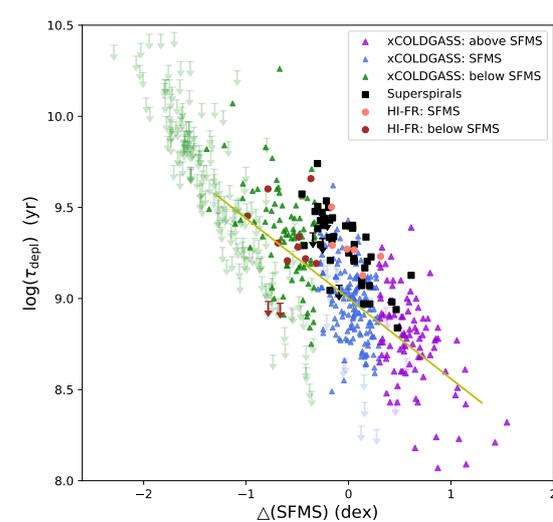
Fig. 9. The gas depletion time $\tau_{dep} = M_{mol}/$SFR as a function of distance to the SFMS for the SS, HI-FR and the COLDGASS sample. The yellow line gives, for illustration, the relation of $\tau_{dep} \propto \triangle(\text{SFMS})^{-0.44}$, (Tacconi et al. 2018).

have a SFR that puts them on the SFMS established from lower-mass galaxies. (ii) They contain large amounts of molecular gas. Adopting a lower than Galactic conversion factor $\alpha_{CO} = 3\ M_\odot/$(K km s^{-1} pc^{-2}) (expected for these high-mass, high-metallicity objects), we find that the molecular gas mass is slightly above what is expected from their mass (extrapolated from lower-mass scaling relations) and roughly what is expected from their distance to the SFMS. (iii) Their molecular gas depletion time is following the mass trend found from lower-mass galaxies, but lies above what is expected from their distance to the SFMS. In the following we are going to discuss how robust these results are and

what we can learn from super spirals with respect to the processes driving galaxy evolution.

4.1. Uncertainties in our analysis

4.1.1. Uncertainties in the molecular gas mass

The molecular gas mass has two uncertainties: The value of the chosen α_{CO} and the redshift correction that we applied. We note that the redshift correction does not affect the molecular gas de-
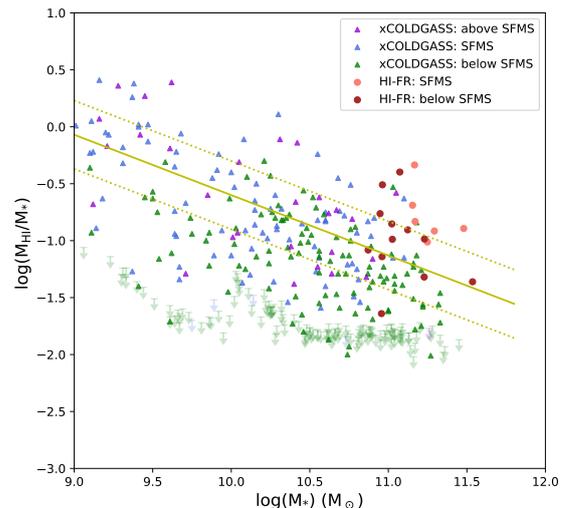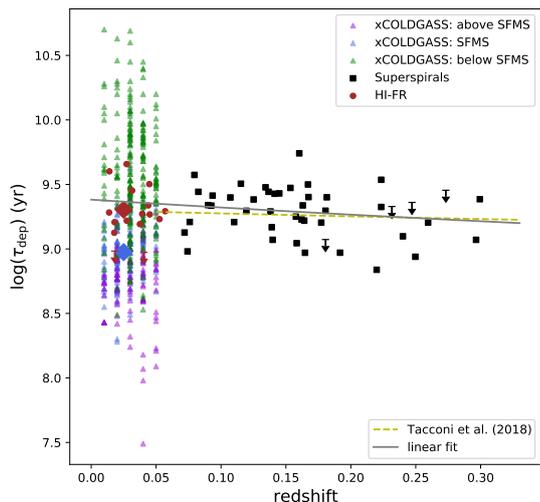
Fig. 10. The gas depletion time $\tau_{dep}= M_{mol}/SFR$ as a function of redshift for the SS, HI-FR and the COLDGASS sample. The yellow line gives, for illustration, the relation of $\tau_{dep} \propto (1-z)^{-0.6}$ from Tacconi et al. (2018), and the gray line is the fit to our data ($\tau_{dep} \propto (1-z)^{-0.02}$). The blue diamond is the mean value of the xCOLDGASS galaxies that lie on the SFMS and the brown diamond is the mean value of the HI-FR sample. The errors of both means are smaller than the symbol size.

pletion time because we use the uncorrected molecular gas mass and SFR to calculate it.

We determined α_{CO} based on its expected metallicity dependence. Both the dependence of α_{CO} on metallicity as well as the derivation of metallicty based on the mass-metallicity relation are somewhat uncertain. We based our choice of α_{CO} on the comparison of different prescriptions, derived from different methods. Accurso et al. (2017) derived their prescription from a combined analysis of [C II] and CO(1-0) data together with radiative transfer modeling. The results from Wolfire et al. (2010), on which the prescription of Bolatto et al. (2013) is based, are from theoretical models of molecular clouds. The difference in α_{CO} between the different studies is only $\sim 20\%$. The influence of the exact value of the metallicity in the high-mass and high-metallicity range is also relatively small because the relation between α_{CO} and metallicity converges to a fixed value (2.9 $M_{\odot}$/(K km s^{-1} pc^{-2}) in the prescription of Bolatto et al. 2013) for high metallicities. Therefore, the uncertainties in α_{CO} due to uncertainties in the metallicity of our objects are not very large, most likely less than 20-30%.

Our choice of α_{CO} depends on the assumption that molecular clouds are on average the same in super spirals as in lower-mass galaxies. More detailed studies are necessary to confirm this assumption, in particular higher resolution observations. There are two parameters that are indicators for possible differences: (i) The distance to the SFMS (Accurso et al. 2017) which determines the intensity of the ultraviolet radiation field that can photo-dissociate CO in the outer layer of molecular clouds. However, this effect is relatively small close to the SFMS. We have tested the prescription of Accurso et al. (2017) by taking into account the distance to the SFMS and found only negligible differences for M_{mol} in our sample. (ii) The total surface density (stars + gas) which is much higher in starburst galaxies, leading to an inter-cloud medium as dense as molecular clouds.
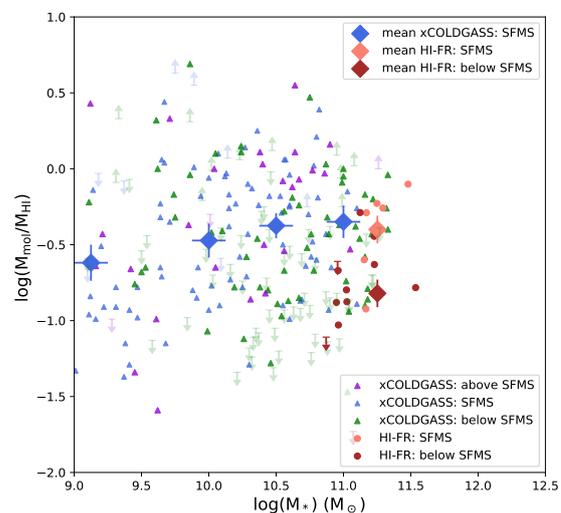
Fig. 11. The atomic gas mass fraction (*upper panel*) and the molecular-to-atomic mass ratio (*lower panel*) as a function of stellar mass for the HI-FR and the xCOLDGASS sample. The mean values of the HI-FR and of the different xCOLDGASS samples are indicated as diamonds, with the length of the vertical bar indicating the error of the mean, and the length of the horizontal bar the width of the chosen mass interval. Only galaxies with detections in HI are considered for the mean value of M_{HI}/M_{mol}. The yellow line in the upper panel indicates the scaling relation found by Janowieski et al. (2020) together with the 0.3 dex width adopted by these authors to characterize the HI main sequence.

This is not the case in our SS+HI-FR sample which are not in a starburst phase and have surface densities in the same range as xCOLDGASS galaxies.

Finally, the molecular gas mass fraction is known to increase with redshift. We have corrected the SS galaxies for this effect, following relations found for other samples, spanning a larger redshift range than SS (Genzel et al. 2015; Tacconi et al. 2018). The resulting z-corrected values for $f_{mol,zcorr}$ (Fig. 3) are left with only a very small dependence on redshift. We therefore consider the redshift correction for the molecular gas mass fraction (as well as for the sSFR) adequate.
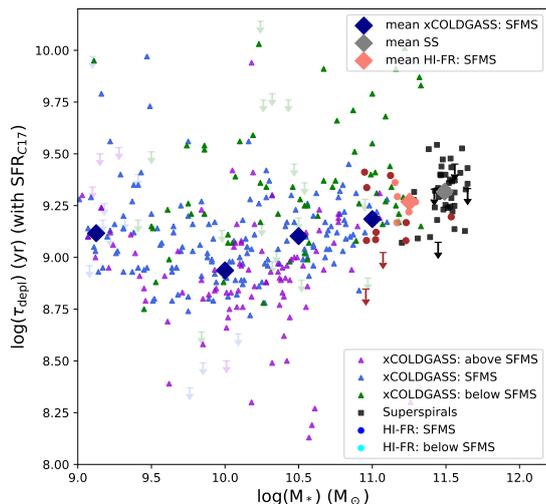
Fig. 12. The gas depletion time $\tau_{dep}= M_{mol}/SFR$ as a function of stellar mass for the super spirals, fast HI rotators and the COLDGASS sample. The SFR has been calculated with the prescription of Cluver et al. (2017), offset by 0.2 dex (eq. 9).


Fig. 13. The gas depletion time $\tau_{dep}= M_{mol}/SFR$ as a function of stellar mass surface density ($\mu_* = M_*/(2\pi r_{p,50,z}^2)$ for the SS, HI-FR and the xCOLDGASS sample.

4.1.2. Uncertainties in SFR and M_*

We derive the SFR with the same prescriptions for both SS and comparison sample in order to avoid biases. In Appendix C we contrast different prescriptions for the calculation of the SFR and conclude that typical uncertainties can be up to 0.1 - 0.2 dex. This small difference does not alter our conclusion that SS galaxies follow the SFMS. In addtion, we can test whether the difference in τ_{dep} between SS and xCOLDGASS galaxies would have been smaller if we had used a different prescription for the SFR. In order to do this, we calculated the SFR for all samples (SS, HI-FR and xCOLDGASS) following the method of Cluver et al. (2017), offset by 0.2 dex (eq. 9), which is the method of those tested in Appendix C with the largest difference. Fig. 12 shows the result. We still find that τ_{dep} of the SS sample is considerably higher than that of xCOLDGASS (see Tab. 6) and that there is a trend of increasing τ_{dep} with stellar mass. Thus, we consider this a robust result.

In Appendix D we compare several methods to calculate M_* and conclude that a constant mass-to-light ratio of $\Upsilon_*^{3.4} = 0.5$ is the best choice for the SS+HI-FR sample, whereas for xCOLDGASS with its wide range of properties, we used, also for consistency with previous studies, the MPA/JHU value provided in Saintonge et al. (2017). In appendix D we concluded that the expected uncertainty is $\sim$ 0.2 dex. This is not expected to affect the conclusion of this paper in a considerable way.

4.2. Super spirals and galaxy evolution

Scaling relations between the gas mass (both atomic and molecular), stellar mass and SFR give insight into how galaxies evolve. The relation between SFR and M_* for star-forming galaxies (the SFMS) has a slope of less than 1, indicating that massive galaxies are not just scaled-up versions of low mass galaxies, instead they presently form less stars per existing stellar mass. There could be various reasons for this trend: (i) a decreasing amount of gas (atomic + molecular) with M_*, (ii) a decreasing amount
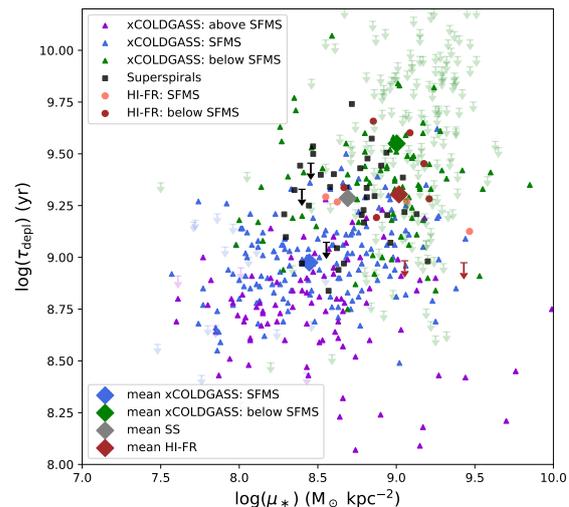
of molecular gas with M_* or (iii) a decreasing efficiency of converting the molecular gas into stars (equivalent to an increasing molecular gas depletion time, τ_{dep}). Both the atomic and the molecular gas fraction decrease with stellar mass, showing that indeed the gas supply is decreasing with stellar mass. In addition, both the atomic and the molecular gas mass decrease below the SFMS (Saintonge et al. 2017). This strongly indicates that the gas supply and in particuar the molecular gas fraction is a driving factor that determines the SFR and the growth of galaxies. Studies of spatially resolved observations confirm this by showing that the surface density of the molecular gas mass correlates stronger with M_* than the SFR, suggesting that the molecular gas is the driving parameter for the SFMS (Lin et al. 2019).

However, not only M_{mol} is a relevant parameter, but also τ_{dep} depends on the position of a galaxy on the SFR-M_* plane. Whereas the dependence on stellar mass is weak, τ_{dep} strongly varies inversely with distance from the SFMS (i.e, it increases below the SFMS). A long depletion time can have different reasons. To start with, CO is a molecule with a low critical density ($\sim$3000 cm^{-3}). This means that it can form in relatively low-density gas, so that molecular gas probed by CO(1-0) might be diffuse, unbound gas of relatively low density, and not necessarily in the form of Giant Molecular Clouds. Another possible reason for the long gas depletion time in massive or below-SFMS galaxies could be a high bulge fraction which can quench SF due to a steep gravitational gradient ("morphological quenching," Martig et al. 2009 or "gravitational quenching," Genzel et al. 2014) or dynamical effects ("dynamical quenching," Gensior et al. 2020). Since the bulge fraction generally increases with stellar mass, this effect could explain the increase of τ_{dep} with M_*. Finally, environmental effects can perturb the gas and affect its ability to form stars as seen in Tidal Dwarf Galaxies (Lisenfeld et al. 2016; Querejeta et al. 2021) or galaxy interactions (Lisenfeld et al. 2017; Braine et al. 2003; Appleton et al. 2022).

How do super spiral galaxies fit into this picture? They are actively star-forming objects, lying on the SFMS which is unusual for their stellar mass. Our observations showed that they

are very gas rich, with molecular gas masses that even put them above the scaling relation extrapolated from lower stellar mass galaxies. This confirms a picture in which the molecular gas mass is a driving factor for maintaining the SF in a galaxy. A second results of our study is that τ_{dep} is longer than for lower-mass galaxies, with SS galaxies following the trend of τ_{dep} with M_* established from lower-mass galaxies, but lying above from what would be expected from their position on the SFMS. This suggests that the efficiency of the molecular gas to form stars is indeed decreasing with stellar mass, even for galaxies on the SFMS.

What could be the reason for the relatively long τ_{dep} in super spiral galaxies? For super spirals a high bulge fraction does not seem to be the reason for the long depletion time because they have on average rather small bulges with bulge-to-total mass ratios mostly between 0.1-0.2 (Ogle et al. 2019b). In Fig. 13 we show the depletion time as a function of stellar mass surface density, $\mu_* = M_*/(2\pi r_{p,50,z}^2)$ with $r_{p,50,z}$ being the radius encompassing 50% of z-band flux band, which is a proxy for the dominance of bulges. Super spirals indeed have high stellar mass surface densities, spanning a wide range between $\log(\mu_*) \approx 8.3 - 9.2\ M_\odot \mathrm{kpc}^{-2}$. This range is, however, entirely in overlap with the surface densities of xCOLDGASS star-forming galaxies which have shorter values of τ_{dep} and also the mean values of μ_* are close (see Tab. 6). On the other hand xCOLDGASS galaxies below the SFMS and FR-HI have considerably higher value of $\log(\mu_*)$. Thus, the difference in τ_{dep} between SFMS xCOLDGASS and SSs does not seem to have it origin in the respective dominance of the bulge. There is no evidence that environmental effects play a role, or that galaxy interactions (although present, as a large fraction of super spirals have multiple nuclei, Ogle et al. 2019a) have had a major impact on their ISM. Possibly the properties of GMCs change in disks of these high stellar mass, but observations with a higher spatial resolution would be necessary to test this.

5. Conclusions

We present and analyze CO(1-0) observations of a sample of 46 super spiral (SS) galaxies, that is to say very massive ($\log(M_*) \gtrsim 11.5\ M_\odot$), actively star-forming disk galaxies. In addition, we include a sample of somewhat less massive disk galaxies with data for the atomic hydrogen and very broad HI spectra from ALFALA (HI fast rotator HI galaxies, HI-FR). These samples are not representative for their mass range, but instead they are rare objects. (Super spirals make up 6 % of the galaxies in their mass range). Their interest consists primarily in their existence and in the fact that the analysis of their properties can provide insights into possible galaxy evolution pathways.

We analyze the relation between SFR, M_* and M_{mol} (and M_{HI} for the HI-FR sample), and compare the properties, after correcting for the expected increase of the SFR and molecular gas fraction. with redshift, to the local sample xCOLDGASS (Saintonge et al. 2017). Our main results are:

- We confirm earlier results (Ogle et al. 2019b) that super spiral galaxies form stars following the SFMS, albeit with values ranging over $\sim$ one order of magnitude in sSFR.
- Our observations show that super SSs contain large amounts of molecular gas. Adopting a conversion factor of $\alpha_{CO}= 3\ M_\odot/(\mathrm{K\ km\ s}^{-1}\ \mathrm{pc}^{-2})$ (which is a factor of 1.4 lower than the Galactic conversion factor, including helium), appropriate for the expected higher metallicity of super spirals, we find a mean (redshift-corrected) molecular gas fraction,

$\log(f_{mol,zcorr}) = -1.36 \pm 0.02$. This molecular gas is higher than expected from the scaling relation with M_* found for xCOLDGASS SFMS galaxies (Janowiecki et al. 2020), but lies well within the scaling relation with the distance from the SFMS.
- The mean value of the gas depletion time, $\log(\tau_{dep}) = \log(M_{mol}/\mathrm{SFR})$ is 9.30 ± 0.03 yr, higher than the value of SFMS xCOLDGASS galaxies in the highest mass bins and following a weak trend with M_* found by other studies (e.g., Saintonge et al. 2017). The depletion times of SS+HI-FR galaxies lies slightly above the relation with the distance from the SFMS for xCOLDGASS galaxies.
- The atomic gas mass fraction ($f_{HI}= M_{HI}/M_*$) of the HI-FR galaxies lies above the scaling relation derived from lower-mass galaxies, which can be explained by a selection effect since we chose galaxies detected by ALFALFA and with broad HI lines. The molecular-to-atomic gas mass ratio of the HI-FR galaxies belonging to the SFMS is in the same range as found for somewhat lower-mass galaxies ($10^{10}\ M_\odot < M_* < 10^{10}\ M_\odot$, suggesting the conversion from atomic to molecular gas proceed in the same way as for lower-mass galaxies.

Our results taken together allow the following conclusions about SF in SSs and galaxy evolution in general:

- A high stellar mass by itself is not a reason for the quenching of SF. If sufficient gas is present - as we found in SS galaxies - and mergers are rare during the lifetime of a galaxies, disk galaxies can grow to large sizes and masses.
- The relation between SFR, M_{mol} and M_* are slightly different than for lower-mass galaxies. Super spiral galaxies are more molecular gas rich than what is expected from their stellar mass, showing that the scaling relations derived from lower-mass galaxies are too steep at this high-mass end. In addition, super spirals have longer molecular gas depletion times than what is expected from their position on the SFMS, suggesting that stellar mass is an additional relevant parameter. The latter results indicates that the properties of the molecular clouds, or the galactic environment in which they are embedded, might be changing as a function of stellar mass.

In conclusion, we find that SSs with their extreme properties allow us to derived more precise scaling relations that can help to better understand SF and galaxy evolution.

References

Accurso, G., Saintonge, A., Catinella, B., et al. 2017, MNRAS, 470, 4750

Appleton, P. N., Emonts, B., Lisenfeld, U., et al. 2022, ApJ, 931, 121

Asplund, M., Grevesse, N., Sauval, A. J., & Scott, P. 2009, ARA&A, 47, 481

Astropy Collaboration, Price-Whelan, A. M., Sipőcz, B. M., et al. 2018, AJ, 156, 123

Astropy Collaboration, Robitaille, T. P., Tollerud, E. J., et al. 2013, A&A, 558, A33

Baldry, I. K., Glazebrook, K., Brinkmann, J., et al. 2004, ApJ, 600, 681

Bettoni, D., Galletta, G., & García-Burillo, S. 2003, A&A, 405, 5

Bianchi, L. 2011, Ap&SS, 335, 51

Blitz, L. & Rosolowsky, E. 2004, ApJ, 612, L29

Blitz, L. & Rosolowsky, E. 2006, ApJ, 650, 933

Bolatto, A. D., Wolfire, M., & Leroy, A. K. 2013, ARA&A, 51, 207

Boquien, M., Buat, V., & Perret, V. 2014, A&A, 571, A72

Boquien, M., Burgarella, D., Roehlly, Y., et al. 2019, A&A, 622, A103

Boselli, A., Cortese, L., & Boquien, M. 2014, A&A, 564, A65

Braine, J., Davoust, E., Zhu, M., et al. 2003, A&A, 408, L13

Brinchmann, J., Charlot, S., White, S. D. M., et al. 2004, MNRAS, 351, 1151

Calzetti, D., Armus, L., Bohlin, R. C., et al. 2000, ApJ, 533, 682

Calzetti, D., Kennicutt, R. C., Engelbracht, C. W., et al. 2007, ApJ, 666, 870

Casasola, V., Bianchi, S., De Vis, P., et al. 2020, A&A, 633, A100

Casasola, V., Cassarà, L. P., Bianchi, S., et al. 2017, A&A, 605, A18

Catinella, B., Saintonge, A., Janowiecki, S., et al. 2018, MNRAS, 476, 875

Chabrier, G. 2003, PASP, 115, 763

Chilingarian, I. V., Melchior, A.-L., & Zolotukhin, I. Y. 2010, MNRAS, 405, 1409

Chilingarian, I. V. & Zolotukhin, I. Y. 2012, MNRAS, 419, 1727

Ciesla, L., Elbaz, D., & Fensch, J. 2017, A&A, 608, A41

Cluver, M. E., Jarrett, T. H., Dale, D. A., et al. 2017, ApJ, 850, 68

Cluver, M. E., Jarrett, T. H., Hopkins, A. M., et al. 2014, ApJ, 782, 90

Dekel, A. & Birnboim, Y. 2006, MNRAS, 368, 2

Di Teodoro, E. M., Posti, L., Fall, S. M., et al. 2022, arXiv e-prints, arXiv:2207.02906

Elbaz, D., Daddi, E., Le Borgne, D., et al. 2007, A&A, 468, 33

Engelbracht, C. W., Rieke, G. H., Gordon, K. D., et al. 2008, ApJ, 678, 804

Eskew, M., Zaritsky, D., & Meidt, S. 2012, AJ, 143, 139

Gensior, J., Kruijssen, J. M. D., & Keller, B. W. 2020, MNRAS, 495, 199

Genzel, R., Förster Schreiber, N. M., Lang, P., et al. 2014, ApJ, 785, 75

Genzel, R., Tacconi, L. J., Lutz, D., et al. 2015, ApJ, 800, 20

Gil de Paz, A., Boissier, S., Madore, B. F., et al. 2007, ApJS, 173, 185

Haynes, M. P., Giovanelli, R., Kent, B. R., et al. 2018, ApJ, 861, 49

Hopkins, P. F., Hernquist, L., Cox, T. J., Robertson, B., & Springel, V. 2006, ApJS, 163, 50

Hunt, L. K., De Looze, I., Boquien, M., et al. 2019, A&A, 621, A51

Hunter, J. D. 2007, Computing in Science & Engineering, 9, 90

Jackson, R. A., Kaviraj, S., Martin, G., et al. 2022, MNRAS, 511, 607

Janowiecki, S., Catinella, B., Cortese, L., et al. 2017, MNRAS, 466, 4795

Janowiecki, S., Catinella, B., Cortese, L., Saintonge, A., & Wang, J. 2020, MN-RAS, 493, 1982

Jarrett, T. H., Chester, T., Cutri, R., et al. 2000, AJ, 119, 2498

Jarrett, T. H., Cluver, M. E., Brown, M. J. I., et al. 2019, ApJS, 245, 25

Jarrett, T. H., Cluver, M. E., Magoulas, C., et al. 2017, ApJ, 836, 182

Jarrett, T. H., Cluver, M. E., Taylor, E. N., et al. 2023, arXiv e-prints, arXiv:2301.05952

Jarrett, T. H., Cohen, M., Masci, F., et al. 2011, ApJ, 735, 112

Jarrett, T. H., Masci, F., Tsai, C. W., et al. 2012, AJ, 144, 68

Jarrett, T. H., Masci, F., Tsai, C. W., et al. 2013, AJ, 145, 6

Kauffmann, G., Heckman, T. M., White, S. D. M., et al. 2003, MNRAS, 341, 54

Kewley, L. J. & Ellison, S. L. 2008, ApJ, 681, 1183

Kroupa, P. 2001, MNRAS, 322, 231

Leroy, A. K., Sandstrom, K. M., Lang, D., et al. 2019, ApJS, 244, 24

Leroy, A. K., Walter, F., Brinks, E., et al. 2008, AJ, 136, 2782

Lin, L., Pan, H.-A., Ellison, S. L., et al. 2019, ApJ, 884, L33

Lisenfeld, U., Alatalo, K., Zucker, C., et al. 2017, A&A, 607, A110

Lisenfeld, U., Braine, J., Duc, P. A., et al. 2016, A&A, 590, A92

Lisenfeld, U., Espada, D., Verdes-Montenegro, L., et al. 2011, A&A, 534, A102

Lisenfeld, U., Verdes-Montenegro, L., Sulentic, J., et al. 2007, A&A, 462, 507

Lisenfeld, U., Xu, C. K., Gao, Y., et al. 2019, A&A, 627, A107

Mannucci, F., Cresci, G., Maiolino, R., Marconi, A., & Gnerucci, A. 2010, MN-RAS, 408, 2115

Martig, M., Bournaud, F., Teyssier, R., & Dekel, A. 2009, ApJ, 707, 250

Meyer, M., Robotham, A., Obreschkow, D., et al. 2017, PASA, 34, 52

Nishiyama, K., Nakai, N., & Kuno, N. 2001, PASJ, 53, 757

Ogle, P. M., Jarrett, T., Lanz, L., et al. 2019a, ApJ, 884, L11

Ogle, P. M., Lanz, L., & Appleton, P. N. 2014, ApJ, 788, L33

Ogle, P. M., Lanz, L., Appleton, P. N., Helou, G., & Mazzarella, J. 2019b, ApJS, 243, 14

Ogle, P. M., Lanz, L., Nader, C., & Helou, G. 2016, ApJ, 817, 109

Pérez, F. & Granger, B. E. 2007, Computing in Science and Engineering, 9, 21

Posti, L., Fraternali, F., & Marasco, A. 2019, A&A, 626, A56

Querejeta, M., Lelli, F., Schinnerer, E., et al. 2021, A&A, 645, A97

Regan, M. W., Thornley, M. D., Helfer, T. T., et al. 2001, ApJ, 561, 218

Saintonge, A. & Catinella, B. 2022, ARA&A, 60, 319

Saintonge, A., Catinella, B., Tacconi, L. J., et al. 2017, ApJS, 233, 22

Saintonge, A., Kauffmann, G., Kramer, C., et al. 2011a, MNRAS, 415, 32

Saintonge, A., Kauffmann, G., Wang, J., et al. 2011b, MNRAS, 415, 61

Salim, S., Boquien, M., & Lee, J. C. 2018, ApJ, 859, 11

Schlafly, E. F. & Finkbeiner, D. P. 2011, ApJ, 737, 103

Schlegel, D. J., Finkbeiner, D. P., & Davis, M. 1998, ApJ, 500, 525

Sivanandam, S., Rieke, M. J., & Rieke, G. H. 2014, ApJ, 796, 89

Solomon, P. M., Downes, D., Radford, S. J. E., & Barrett, J. W. 1997, ApJ, 478, 144

Speagle, J. S., Steinhardt, C. L., Capak, P. L., & Silverman, J. D. 2014, ApJS, 214, 15

Tacconi, L. J., Genzel, R., Saintonge, A., et al. 2018, ApJ, 853, 179

Tacconi, L. J., Genzel, R., & Sternberg, A. 2020, ARA&A, 58, 157

van der Walt, S., Colbert, S. C., & Varoquaux, G. 2011, Computing in Science and Engineering, 13, 22

Verdes-Montenegro, L., Sulentic, J., Lisenfeld, U., et al. 2005, A&A, 436, 443

Virtanen, P., Gommers, R., Oliphant, T. E., et al. 2020, Nature Methods, 17, 261

Wolfire, M. G., Hollenbach, D., & McKee, C. F. 2010, ApJ, 716, 1191

Wong, T. & Blitz, L. 2002, ApJ, 569, 157

Yao, H. F. M., Cluver, M. E., Jarrett, T. H., et al. 2022, ApJ, 939, 26

Appendix A: CO(1-0) spectra of central pointings

Appendix A: CO(1-0) spectra of central pointings
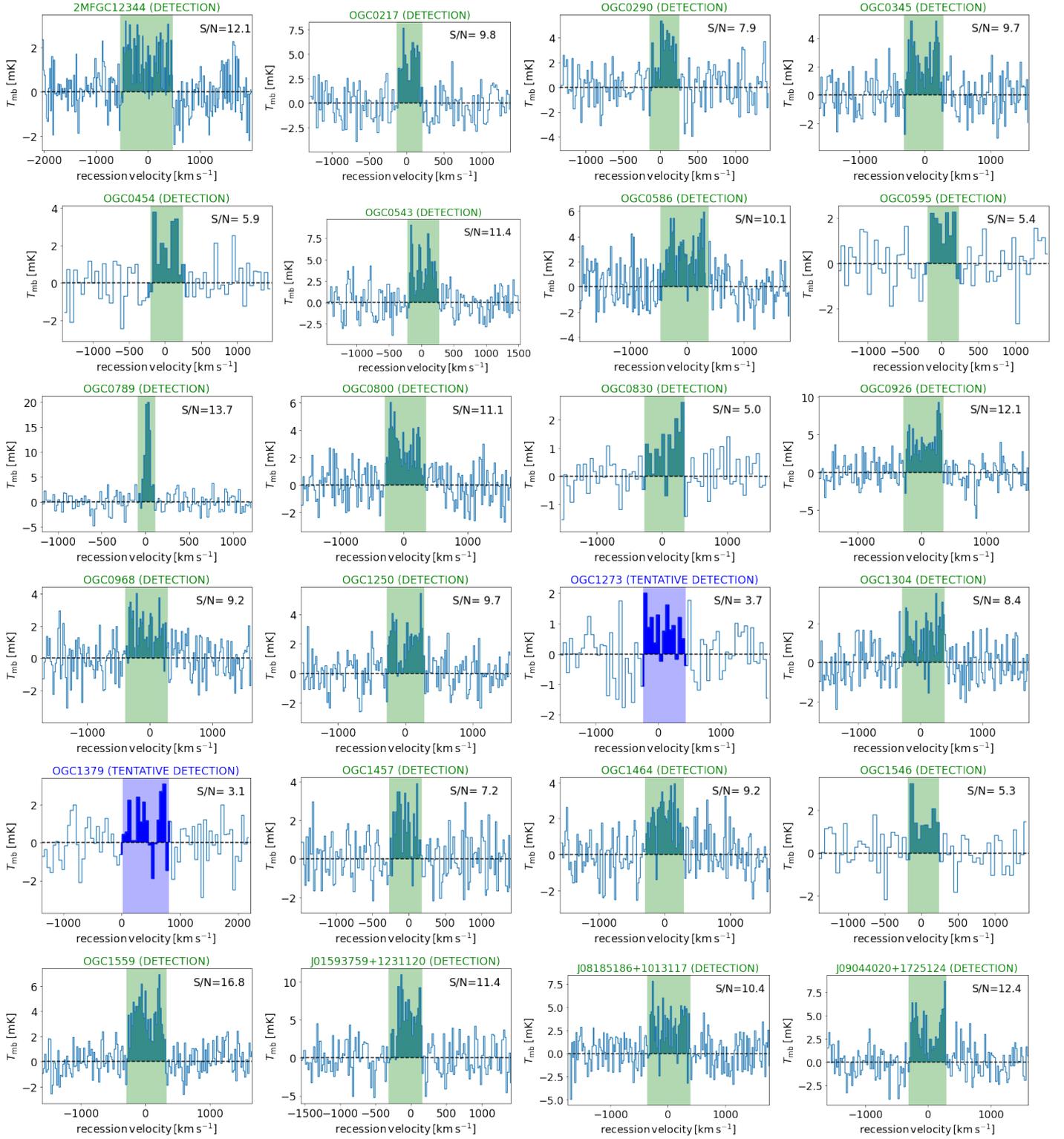
Fig. A.1. Observed spectra of the SS galaxies. The signal-to-noise ratio S/N = I_{CO}/error(I_{CO}) is indicated in the upper left corner. The velocity resolution is 20 km s^{-1} for objects with S/N ≳ 7 and 50 km s^{-1} for objects with S/N ≲ 7 . The x-axis gives the velocity relative to the (optical) recession velocity, $v_{rec} = cz$, where z is the SLOAN redshift. The coloured shaded area represents the region over which the line is integrated to determine the total flux.
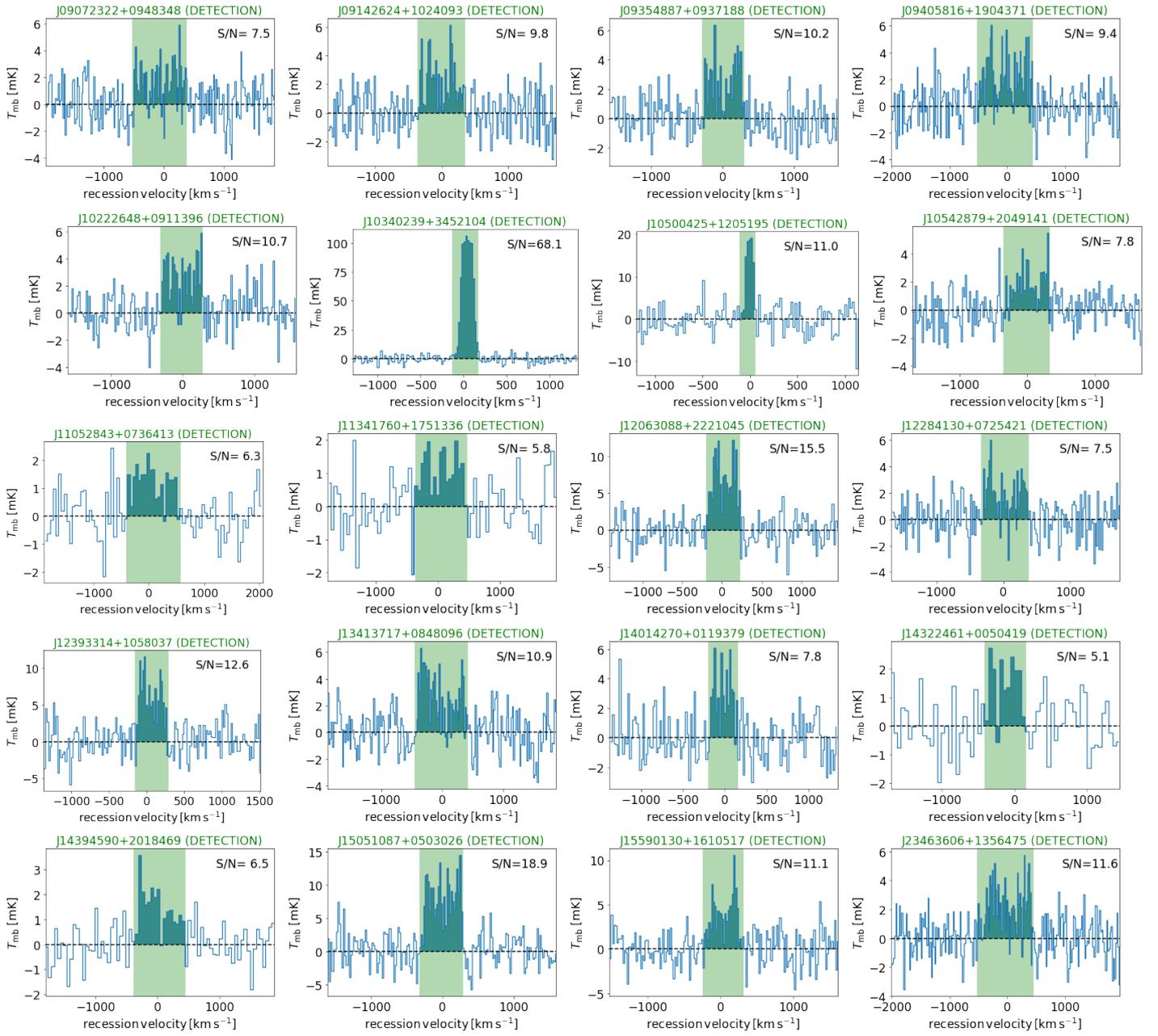
Fig. A.1. continued
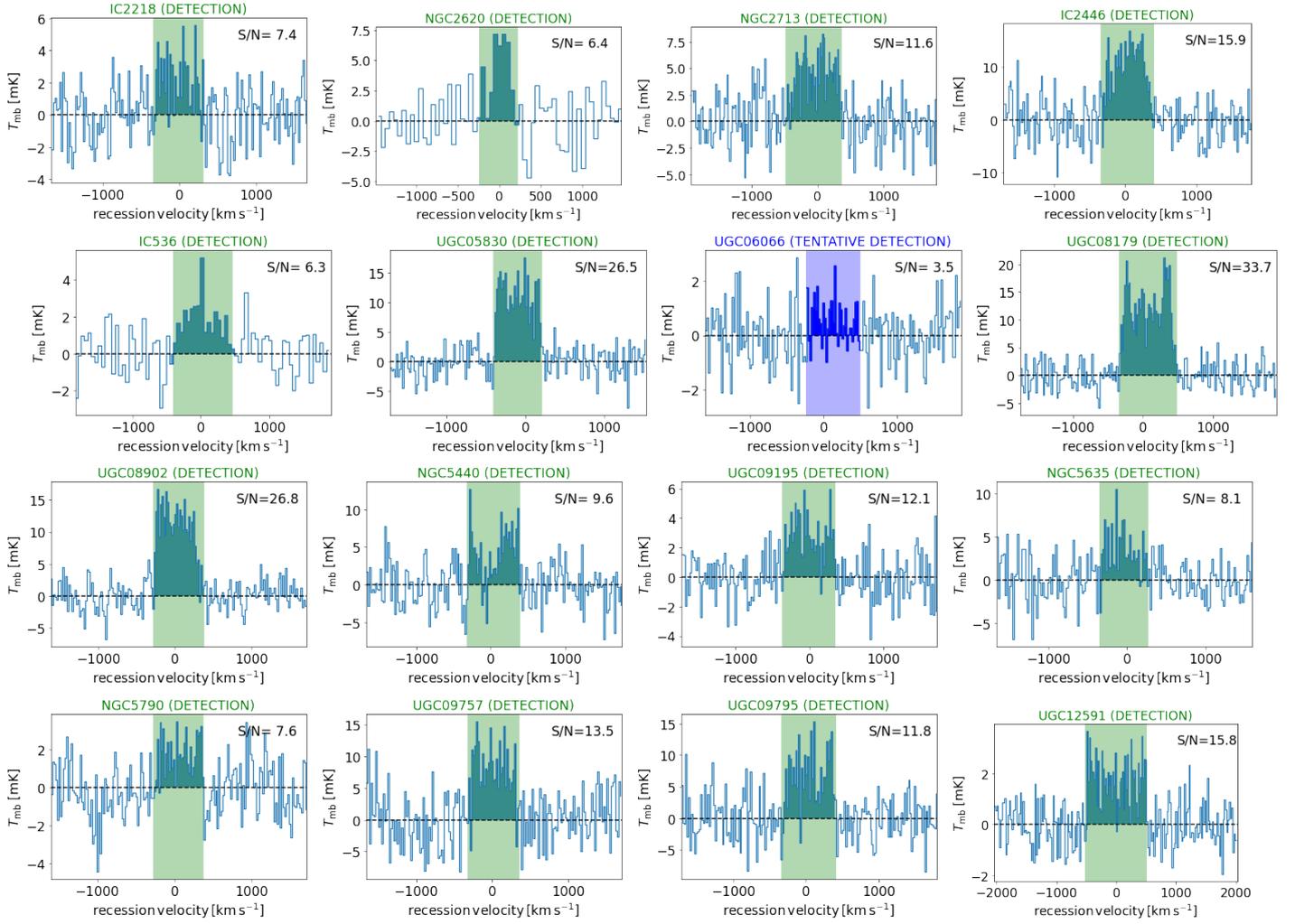
Fig. A.2. Observed spectra of the HI-FR galaxies. The signal-to-noise ratio S/N = I_{CO}/error(I_{CO}) is indicated in the upper left corner. The velocity resolution is 20 km s^{-1} for objects with S/N $\gtrsim$ 7 and 50 km s^{-1} for objects with S/N $\lesssim$ 7 . The x-axis gives the velocity relative to the (optical) recession velocity, $v_{rec} = cz$, where z is the SLOAN redshift. The coloured shaded area represents the region over which the line is integrated to determine the total flux. The spectra are for the central emission, except for NGC 2713, NGC 5790, UGC 08902 and UGC 12591 for which the spectrum averaged over the positions along the major axis are shown.
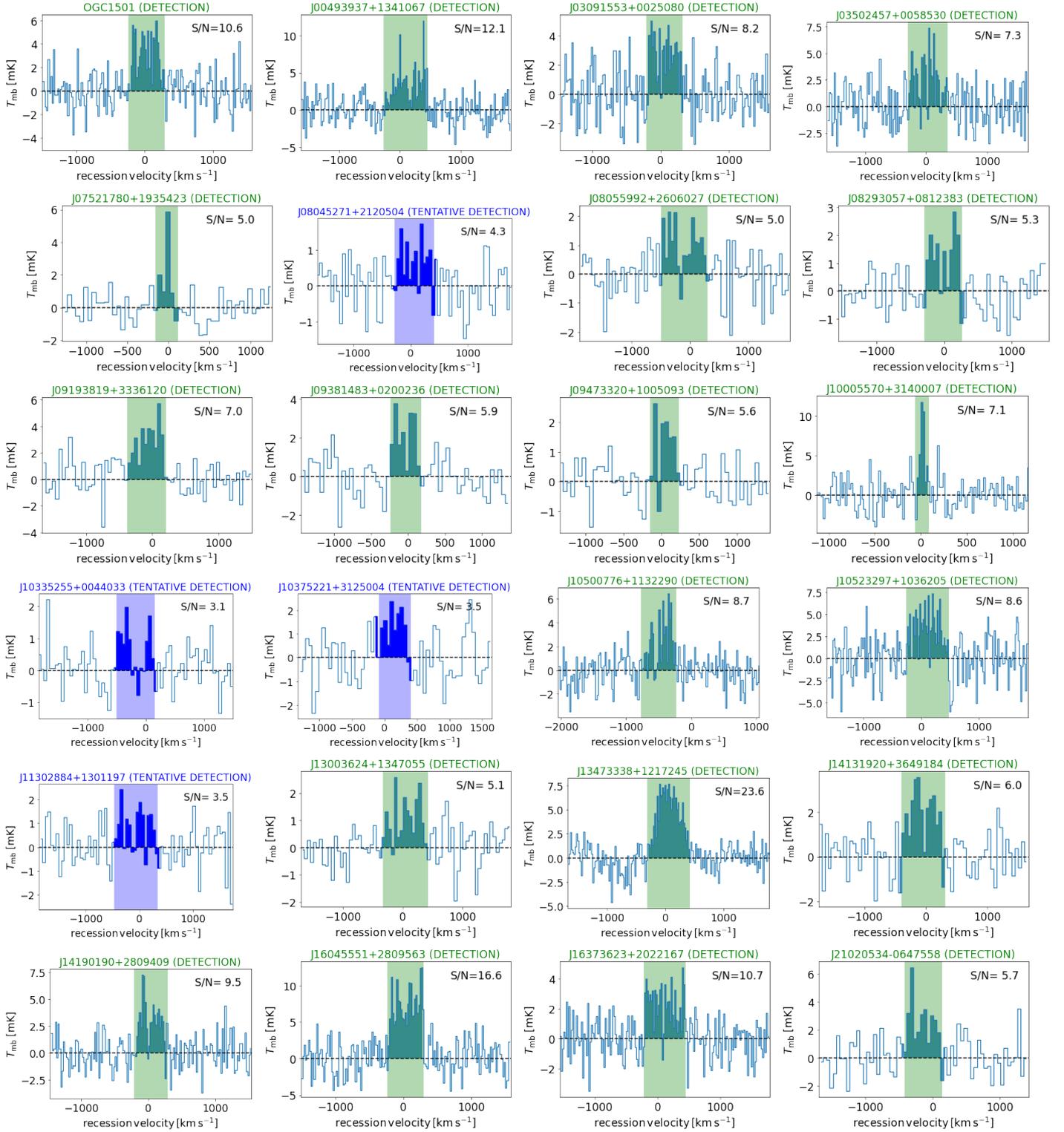
Fig. A.3. Observed spectra of AGNs. The signal-to-noise ratio S/N = I_{CO}/error(I_{CO}) is indicated in the upper left corner. The velocity resolution is 20 km s^{-1} for objects with S/N $\gtrsim$ 7 and 50 km s^{-1} for objects with S/N $\lesssim$ 7 . The x-axis gives the velocity relative to the (optical) recession velocity, $v_{rec} = cz$, where z is the SLOAN redshift. The coloured shaded area represents the region over which the line is integrated to determine the total flux.

Appendix B: Mapped galaxies
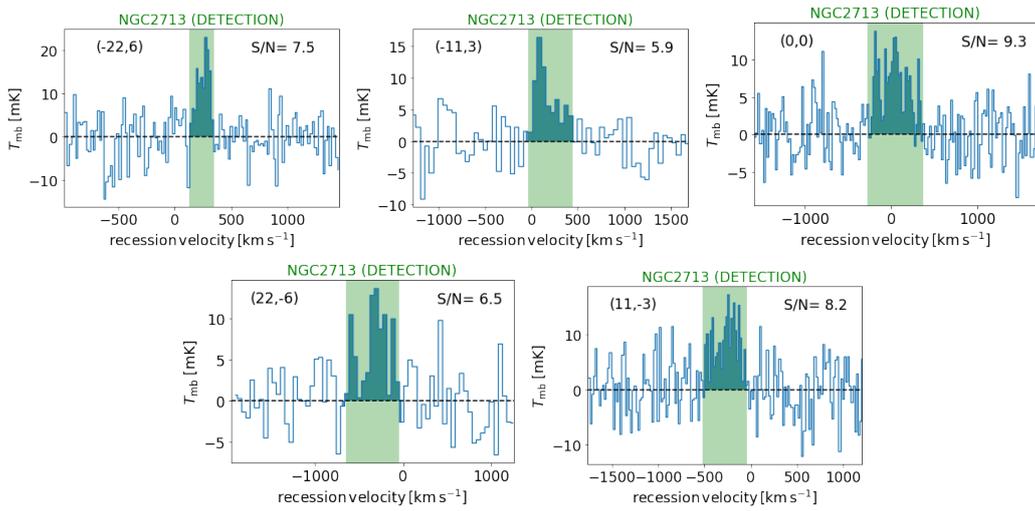
Fig. B.1. Observed spectra along major axis of NGC 2713. The velocity resolution is 20 km s^{-1} for objects with S/N $\gtrsim$ 7 and 50 km s^{-1} for objects with S/N $\lesssim$ 7. The offset in arcsec is given in the upper left corner.
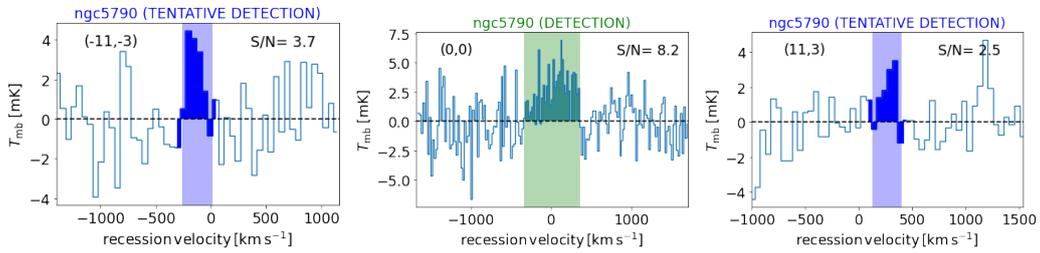
Fig. B.2. Observed spectra along major axis of NGC 5790. The velocity resolution is 20 km s^{-1} for objects with S/N $\gtrsim$ 7 and 50 km s^{-1} for objects with S/N $\lesssim$ 7. The offset in arcsec is given in the upper left corner.
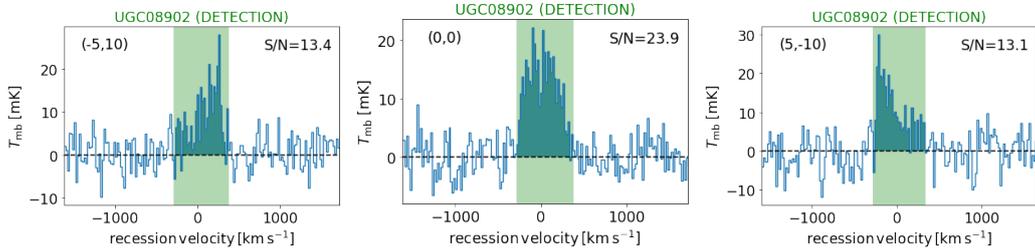
Fig. B.3. Observed spectra along major axis of UGC08902. The velocity resolution is 20 km s^{-1}. The offset in arcsec is given in the upper left corner.
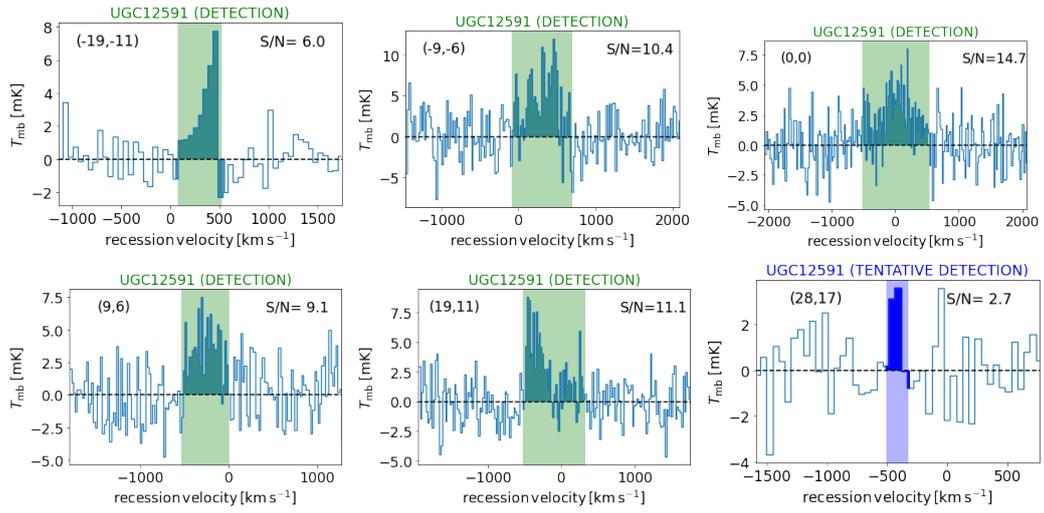
Fig. B.4. Observed spectra along major axis of UGC 12591. The velocity resolution is 20 km s^{-1} for objects with S/N $\gtrsim$ 7 and 50 km s^{-1} for objects with S/N $\lesssim$ 7. The offset in arcsec is given in the upper left corner.

Appendix C: Comparison of methods to calculate the SFR

In order to measure the SFR, the most reliable methods combine direct emission from massive stars (as UV or Hα) and emission from dust to probe dust-enshrouded SF. For massive galaxies, the second part is usually dominant so that methods that solely rely on the dust emission give very reliable results as well. In this section, we are going to compare the hybrid SFR tracer SFR$_{\text{best}}$ (see Sect. 2.7.1) to the hybrid SFR tracer from Leroy et al. (2019) and the monocromatic SFR tracer from Cluver et al. (2017).

Both the WISE W3 and the W4 bands can be used as sensitive SF tracers. Cluver et al. (2017) derived monocromatic SFR prescription for both the W3 and W4 band for the combined SINGS and KINGFISH sample. They showed that W3 is an excellent tracer for the SFR. In contrast to the *Spitzer* 8 μm band, which is dominated by PAH emission (Calzetti et al. 2007; Engelbracht et al. 2008), the WISE W3 band at 11 μm only has

a contribution of $\sim 30\%$ PAH emission, the rest being hot dust and stellar emission. Therefore, after correction for the stellar emission, Cluver et al. (2017) found a lower scatter for the SFR derived from W3 compared to the SFR derived from the stellar-continuum corrected W4 band. Here, we use the prescription based on the stellar-continuum subtracted W3 emission following eq. 9.

Leroy et al. (2019) derived the coefficients for the SFR prescription based on GALEX and WISE data for a sample of $\sim 100\,000$ galaxies with masses up to $\sim 10^{11}$ $M_\odot$ by comparing the luminosities to SFRs derived from CIGALE by Salim et al. (2018). Due to the large number of galaxies in their sample they could study trends of these coefficients with respect to other parameters as the stellar mass, WISE colours or the sSFR. In contrast to Cluver et al. (2017), they found that the W4 band has a higher stability as a SFR tracer, i.e. that the W4 coefficients depend less on other parameters than for W3. This difference between Cluver et al. (2017) and Leroy et al. (2019) might be due to the fact that the Leroy prescriptions are based on the total WISE luminosities, i.e. without subtracting the stellar continuum. The stellar continuum has a larger contribution in the W3 than in the W4 band. Thus, the higher dependence of W3 on other parameters found by Leroy et al. (2019) might in reality be the effect of a varying stellar contribution in the W3 band. Taking both studies into account, we conclude that both the W3 and W4 band are reliable tracers for the SFR, especially when a correction for the stellar continuum is done. We test the prescription of Leroy et al. (2019), based on W3, W4 and NUV (their Table. 7):

$$SFR_{W4+NUV,L19}[M_\odot \text{yr}^{-1}] = L_{\text{NUV}}10^{-43.24} + L_{\text{W4,dust}}10^{-42.79} \quad \text{(C.1)}$$

$$SFR_{W3+NUV,L19}[M_\odot \text{yr}^{-1}] = L_{\text{NUV}}10^{-43.24} + L_{\text{W3,dust}}10^{-42.86} \quad \text{(C.2)}$$

In Figs. C.1-C.3 we show the results. The comparison of SFR$_{\text{best}}$ with SFR$_{W4+NUV,L19}$ is excellent except for a few outliers. This is not too surprising since the coefficients of the prescriptions are very similar, the only difference being that the Leroy et al. prescription is based on the total W3 and W4 luminosities, whereas the Janowiecki et al. prescription is based on the W3 and W4 luminosities from dust only. The contribution from dust is higher for the W3 luminosity so that the comparison of SFR$_{\text{best}}$ and SFR$_{W3+NUV,L19}$ (Fig. C.2) presents a larger scatter. We can also see a trend that galaxies with a more quiescent stellar population (as galaxies below the SFMS in the xCOLDGASS and the FR-HI sample) have higher values of the SFR from the Leroy et al. prescription compared to SFR$_{\text{best}}$. This is due to their higher L_{W1}/L_{W3} values and therefore the higher stellar contribution in the W3 band. But in general, also for SFR$_{W3+NUV,L19}$, the agreement between both prescriptions is good.
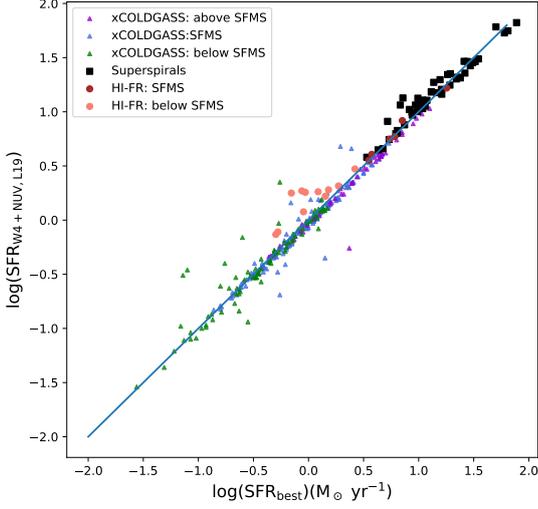
Fig. C.1. Comparison of SFR$_{best}$ to the prescription of Leroy et al. (2019) (see eq. C.1). The blue line is the unity line to guide the eye.
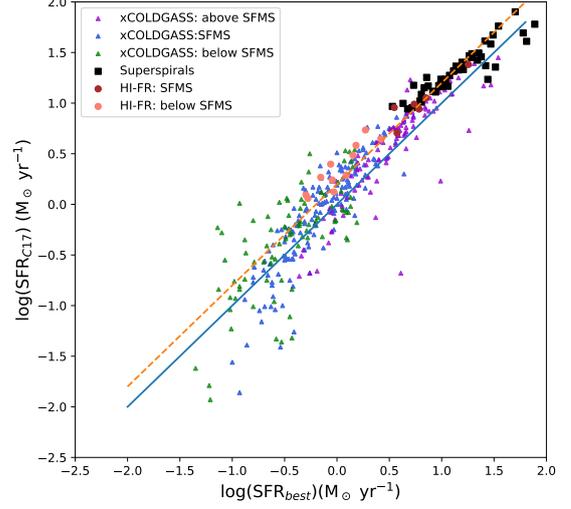

Fig. C.3. Comparison of SFR$_{best}$ to the prescription of Cluver et al. (2017) (see eq. 9). The blue line is the unity line to guide the eye, and the yellow dashed line is offset by 0.2 dex, corresponding to the mean value of log(SFR$_{W3,C17}$/SFR$_{best}$).

The comparison with the Cluver et al. (2017) prescription also shows a good agreement, albeit with a constant offset of ∼ 0.2 dex. Towards lower SFRs there is a trend of lower values of SFR$_{W3,C17}$ compared to SFR$_{best}$ which is most likely due to a larger contribution of dust-unobscured SF.

In Tab. C.1 we list the mean values and standard deviation of the ratio between the different tracers for the different subgroups. The standard deviation gives us an idea of the general uncertainty in the calculation of the SFR, and the differences in the mean values for the different sample an idea of the uncertainty when comparing the results between different groups. In general, we find a satisfactory agreement between the different tracers with roughly linear relations between them (see Figures). There are some differences in the mean values of the ratio between the different groups, with differences up to 0.20 - 0.25 dex between SF and quiscient subsamples, but less (up to ∼ 0.1 dex) between the SFMS samples. This means that there could be artificial differences up to this order of magnitude in the mean SFR when comparing these subsamples.

Fig. C.2. Comparison of SFR$_{best}$ to the prescription of Leroy et al. (2019) (see eq. C.2). The blue line is the unity line to guide the eye.

Table C.1. Comparison of different methods to calculate the SFR

Sample	log($\frac{SFR_{W4+NUV,L19}}{SFR_{best}}$) mean (stdv)^a	log($\frac{SFR_{W3+NUV,L19}}{SFR_{best}}$) mean (stdv)^a	log($\frac{SFR_{W3,C17}}{SFR_{best}}$) mean (stdv)^a
SS	0.03 (0.08)	0.03 (0.14)	0.17 (0.14)
FR-HI	0.12 (0.12)	0.22 (0.16)	0.29 (0.12)
xCOLDGASS (SFMS)	-0.03 (0.09)	-0.03 (0.13)	0.05 (0.25)
xCOLDGASS (below SFMS)	0.02 (0.15)	0.22 (0.22)	0.06 (0.48)

Notes. $^{(a)}$ Mean value and standard deviation (in parenthesis).

Appendix D: Comparison of different methods to calculate M_*

We compared several prescriptions to calculate the stellar mass:

– A constant mass-to-light ratio, $\Upsilon_*^{3.4} = 0.5$. Whereas this is too simplistic for the entire sample, it is a reasonable assumption to test for the rather homogeneous sample of massive spirals.
– The method of Cluver et al. (2014) who derive a color dependent $\Upsilon_*^{3.4}$ based on the analysis of a sample of galaxies with GAMA data for which the stellar mass was derived from an analysis of stellar populations. Their best-fit prescription for the entire sample (their eq. 2) is:

$$\log(M_{*,C14}/L_{W1})[M_\odot/L_{W1,\odot}] = -1.96(W1 - W2) - 0.03,$$
$$(D.1)$$
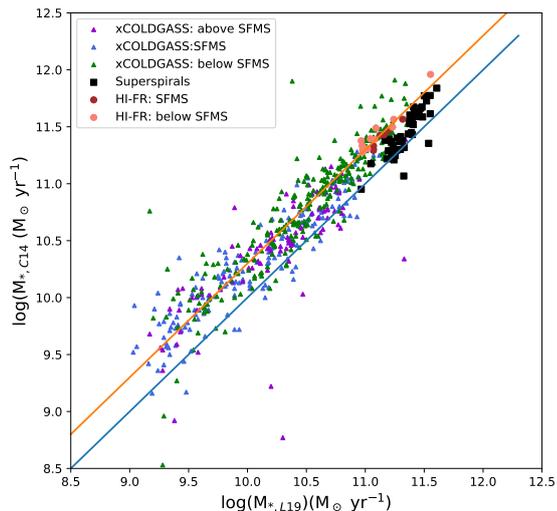
Fig. D.1. Comparison of the stellar mass derived from the methods of Cluver et al. (2014) and Leroy et al. (2019). The blue line is the unity line to guide the eye and the yellow line is offset by 0.3 dex which corresponds to the mean value of $\log(M_{*C14}/M_{*L19})$ for the quiescent subsamples (see Tab. D.1).
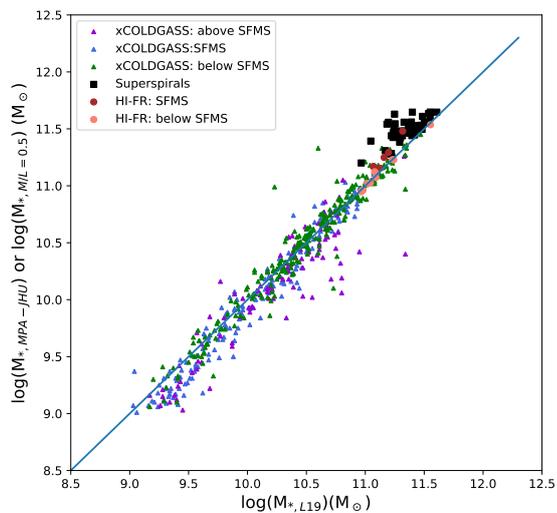

Fig. D.2. Comparison of the stellar mass derived from the method of Leroy et al. (2019), and MPA/JHU for the xCOLDGASS sample, respectively a constant $\Upsilon_* = 0.5$ for the SS+FR-HI sample. The blue line is the unity line to guide the eye.

where $(W1 - W2)$ is the WISE color in mag.

– Leroy et al. (2019) compared for a sample of $\sim$ 130.000 galaxies the stellar mass derived from fitting the UV-to-mid-infrared spectral energy distribution (SED) with CIGALE from Salim et al. (2018) to different observationally derived parameters (SFR, WISE luminosities and colours).

Table D.1. Comparison of different methods to calculate the stellar mass

Sample	$\log(\frac{M_{*,C14}}{M_{*,L19}})$ mean (stdv)[a]	$\log(\frac{M_{*,MPA/JHU}}{M_{*,L19}})$ mean (stdv)[a]	$\log(\frac{M_{*,\Upsilon_{*0.5}}}{M_{*,L19}})$ mean (stdv)[a]
SS	0.11 (0.11)	–	0.14 (0.10)
FR-HI	0.31 (0.05)	–	0.03 (0.06)
xCOLDGASS (SFMS)	0.21 (0.28)	-0.08 (0.16)	–
xCOLDGASS (below SFMS)	0.31 (0.22)	0.01 (0.12)	–

Notes. [a] Mean value and standard deviation (in parenthesis).

The best correlation for $\Upsilon_*^{3.4}$ that they obtained was with $\text{SFR}/\nu L_\nu(W1)$ (their eq. 24, see also their Figs. 22 and 23):

$$\Upsilon_*^{3.4}[M_\odot/L_{W1,\odot}] = \begin{cases} 0.5, & \text{if } Q < a \\ 0.5 + b\,(Q-a), & \text{if } a < Q < c \quad \text{(D.2)} \\ 0.2, & \text{if } Q > c \end{cases}$$

where $L_{W1,\odot} = 1.6 \cdot 10^{32}$ erg s^{-1} = 0.042 $L_\odot$ is the Solar luminosity in the W1 (3.4 μm) band, $a = -11$, $b = -0.21$ and $c = -9.5$ (see Table 6 in Leroy et al. 2019). Q = $\text{SFR}/\nu L_\nu(W1)$ with $\nu L_\nu(W1)$ being the luminosity in the W1 in units of solar bolometric luminosity ($L_\odot$). Given that $\nu L_\nu(W1)$ is closely related to the stellar mass, Q is a quantity that is similar to the sSFR. This prescription gives a high value (0.5 $M_\odot/L_{W1,\odot}^{-1}$) for quiescent galaxies and a low value (0.2 $M_\odot L_{W1,\odot}^{-1}$) for actively star-forming objects. Applying this method to the SS sample, values for $\Upsilon_*^{3.4}$ between 0.25 and 0.5 were derived.

Fig. D.1 shows the comparision of the method of Cluver et al. (2014) and Leroy et al. (2019). A good correlation is visible, albeit with an difference of 0.1-0.3 dex between both methods. This offset is similar for all subsamples except for SSs for which $M_{*,C14}/M_{*,L19}$ is $\sim$ 0.1 dex lower than for the star-forming galaxies in xCOLDGASS (see Tab. D.1). This means that either the method of Leroy et al. overpredict the true stellar mass of super spirals, or Cluver et al. underpredicts it. The difference is, however, small.

Fig. D.2 shows the comparison of the methods of Leroy et al. (2019) and the stellar masses from the MPA/JHU catalog for xCOLDGASS galaxies and a constant $\Upsilon_*^{3.6} = 0.5$ for the SS+FR-HI sample. The agreement between both methods is satisfactory (see Tab. D.1). For the quiescent xCOLDGASS galaxies and for the FR-HI the agreement is perfect, whereas the mean value of $M_{*,MPA/JHU}$ for SFMS xCOLDGASS galaxies is slightly (0.08 dex) lower than the value from Leroy et al. (2019) and for SS galaxies the mean value for M_* derived with a constant $\Upsilon_*^{3.4} = 0.5$ for SS galaxies is slightly higher (0.14 dex) than the value from Leroy et al. (2019). Overall, the differences are small and close to the standard deviation of the ratios (see Tab. D.1).

Appendix E: SED fitting of the SS galaxies with CIGALE

CIGALE (Code Investigating GALaxy Emission; Boquien et al. 2019) is a python implemented code based on an energy balance
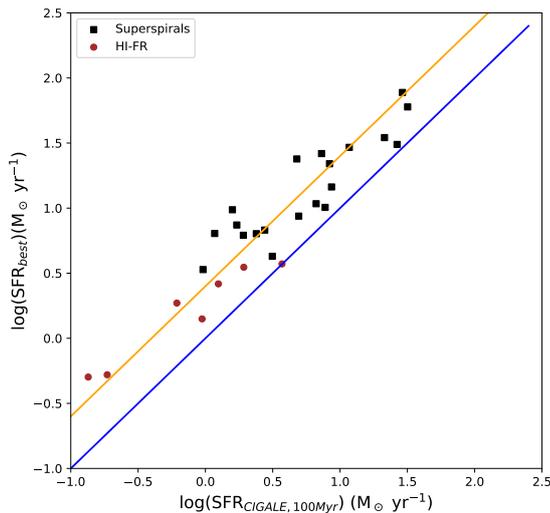
Fig. E.1. Comparison of SFR$_{best}$ and SFR averaged over the past 100 Myr derived by CIGALE. The blue line shows unity to guide the eye and the yellow line is offset by 0.4 dex which corresponds to the mean value of log(SFR$_{best}$/SFR$_{CIGALE,100Myr}$).
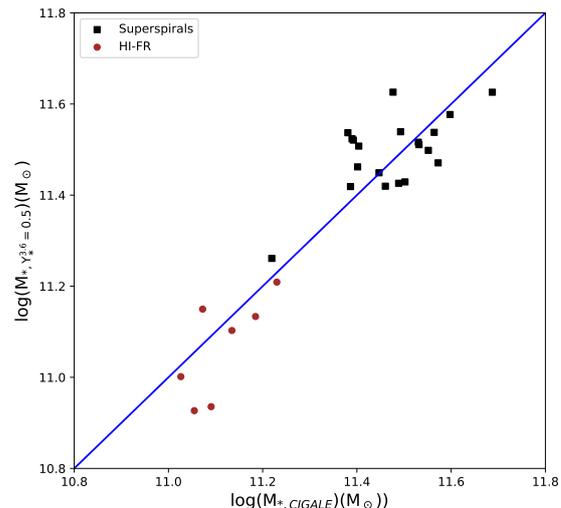

Fig. E.2. Comparison of M_* derived by CIGALE and M_* derived from the W1 luminosity assuming a $\Upsilon_*^{3.6} = 0.5$. Only objects with a good fit (reduced $\chi^2 < 1$) are taken into account. The blue line shows unity.

principle, where the energy absorbed by dust from UV to near-infrared frequencies is re-emitted in the mid- and far-infrared. It has a Bayesian-like approach and has allowed us to model the SED of our SS+FR-HI galaxy sample from far-UV up to far-infrared wavelengths, and to estimate their physical properties, such as SFR and stellar mass. For reliability purposes, only objects with $\chi^2 < 1$ have been considered during the analysis.

For the data input, we used the GALEX and WISE data presented in this paper (without the k-correction since CIGALE performs a k-correction in the fitting process), together with SDSS fluxes for the u, g, r, i and z-band. For the GALEX and WISE data we added to the photometric errors a calibration error in quadrature (14.8 % for GALEX, Gil de Paz et al. 2007, and 2.4%, 2.8%, 4.5%, and 5.7% for the W1, W2, W3, and W4 images, respectively, Jarrett et al. 2011).

To perform the fits we used a series of modules that model the SF history (SFH), stellar population, nebular emission, dust attenuation, and dust emission. The modules and parameters used in our fits follow those used by Hunt et al. (2019), detailed in Table 1 of their article, with the exception of two parameters that have been slightly modified to model our sample better:

1. The SFH is modeled using a delayed + truncated parametrization (Ciesla et al. 2017), where $r_{SFR} = SFR(t > t_{trunc})/SFR(t_{trunc})$ considers a reduction or increase in the SFR after the truncation time, t_{trunc}. We allow the parameter set $r_{SFR} = (0.01, 0.05, 0.1, 0.5, 1.5, 10)$.
2. We choose a modified starburst attenuation law (Calzetti et al. 2000) that considers different attenuations for stellar populations of different ages. The baseline law is multiplied by λ^δ, where we select the following values for the power-law slope, $\delta = (-1.0, -0.8, -0.6, -0.4, -0.2, 0.0)$.

The mean values and standard deviations of the ratios between the value derived from CIGALE and from the prescriptions used here are given in Tab. E.1

Fig. E.1 gives a comparison between the SFR derived with CIGALE (averaged over the past 100 Myr) and SFR$_{best}$ for ob-
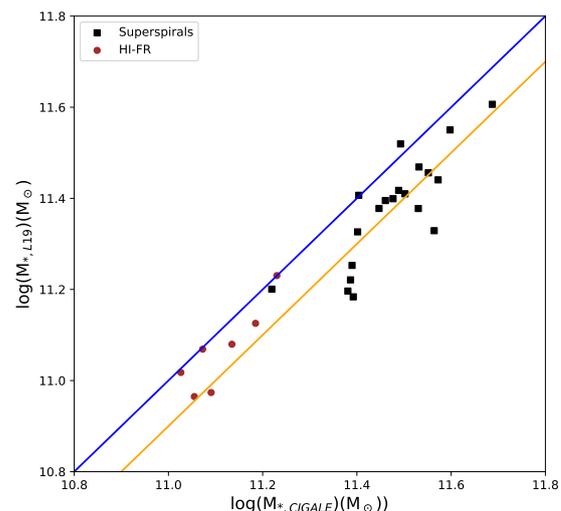

Fig. E.3. Comparison of M_* derived by CIGALE and M_* following the prescription of Leroy et al. (2019). Only objects with a good fit (reduced $\chi^2 < 1$) are taken into account. The blue line shows unity and the orange line an offset of -0.1 dex.

jects with a good fit (reduced $\chi^2 < 1$). A good correlation is visible, albeit offset by 0.4 dex (which is the mean value of log(SFR$_{CIGALE,100Myr}$/SFR$_{best}$)). The offset most likely reflects the different definitions of both SFRs, as the SFR traced by UV+WISE data is not exactly the same as the SFR averaged over the past 100 Myr (see Boquien et al. 2014, for a detailed discussion of the time-scales of SFRs derived from different tracers). The standard deviation of the correlation is 0.2 dex which gives an estimate for the uncertainty of the determination of the SFR.

Fig. E.2 shows the comparison between the stellar mass derived from CIGALE and the value derived with a constant mass-to-light ratio, $\Upsilon_*^{3.4} = 0.5$ and Fig. E.3 the comparison of CIGALE

Table E.1. Comparison of SFR and M_* from CIGALE and different methods

Sample	$\log(\frac{SFR_{best}}{SFR_{CIGALE,100Myr}})$ mean (stdv)^a	$\log(\frac{M_{*,L19}}{M_{CIGALE}})$ mean (stdv)^a	$\log(\frac{M_{*,\Upsilon_*^{3.4}=0.5}}{M_{CIGALE}})$ mean (stdv)^a
SS	0.41 (0.21)	-0.09 (0.07)	0.03 (0.08)
FR-HI	0.37 (0.20)	0.01 (0.03)	0.01 (0.05)

with the values derived from the prescription of Leroy et al. (2019) (eq. D.2.) In both cases, good correlations exist. In the case of the Leroy et al. prescription there is a small, relatively constant offset between both measurement, with CIGALE giving a slightly (by 0.1 dex) higher value for M_* (see Tab. E.1). We also compared the prescription by Cluver et al. (2014) to CIGALE (not shown) and obtained a larger scatter (standard deviation 0.19). We conclude that both the calculation of Leroy et al. (2019) and a constant mass-to-light ratio $\Upsilon_*^{3.4} = 0.5$ give a good agreement with CIGALE. Taking the standard deviation as a reference, the uncertainty in the estimate of M_* is 0.1-0.2 dex.